



מכון ויצמן למדע

Weizmann Institute of Science

Thesis for the degree
Philosophy Doctor

by
Hagai Eisenberg

חבור לשם קבלת התואר
דוקטור לפילוסופיה

מאת
חגי איזנברג

Nonlinear Effects in Waveguide Arrays

תופעות אי-ליניאריות במערכים של מוליכי-גלים

November 2002

Submitted to the Council of the
Weizmann Institute of Science
Rehovot, Israel

כסלו תשס"ג

מוגש למועצה המדעית של
מכון ויצמן למדע
רחובות, ישראל

Preface

Solitons are not a new phenomena. They were already observed about 170 years ago as a stable water levitation in a narrow and shallow canal. It was not until the beginning of the 1970's that this phenomenon was associated with optics, following the introduction of lasers and the discovery of nonlinear self-focusing of intense beams during the previous decade. Two forms of optical solitary waves have been proposed. The first are optical *spatial* solitons that appear as beams whose diffraction is exactly compensated by self-focusing. The second form are optical *temporal* solitons, realized by light pulses whose broadening due to chromatic dispersion is exactly balanced by self-phase modulation. Both nonlinear effects are results of the Kerr nonlinearity. Various categories of optical solitons were introduced since their first proposal. They are different from each other by their dimensionality, the nonlinearity which forms the solitons, other nonlinear effects that accompany their creation, coherence and other factors.

During the last six years, I had the opportunity to study two branches of the soliton tree. In my M.Sc. work I began researching numerically the self-focusing of spatiotemporal pulses, and towards the end of my Ph.D. period I revisited this phenomena, but from an experimental point of view. However, the main trunk of my thesis stems from a different direction. Thanks to the fruitful collaboration that our group has with Prof. Stewart Aitchison from Glasgow (now in Toronto) and his resourceful student Dr. Roberto Morandotti, I concentrated mainly on waveguide arrays. We were the first to demonstrate *Discrete Solitons*, and performed many experiments in this field. Our interest in waveguide arrays grew and flourished also towards some linear effects that occur in such waveguides.

This thesis is organized as follows: We start in the first chapter by describing some theoretical background about dynamics of discrete linear and nonlinear optical fields. The next chapter includes our experimental results with discrete solitons. In the third chapter, three works about linear dynamics in various designs of waveguide arrays are presented. We conclude with a report of the spatiotemporal focusing experiment in a slab waveguide, which we also refer to as the Kerr *light-bullets* experiment.

I was truly lucky to meet Prof. Yaron Silberberg at about the same time as he arrived at the Weizmann Institute. I was his first M.Sc. student and I can not compare my knowledge at the day I entered his lab to this day when I'm leaving him. He enriched me with a wide variety of scientific approaches and methods which will serve me for many years. For that, I try to thank him here.

Two weeks after the official starting date of my Ph.D., another tree was planted. My wife Helen and I were married and the help and support that she gave me along my Ph.D. period is invaluable and can not be expressed by words. Meanwhile, two young twigs came out of our modest tree, namely Eran and Hillel. Their contribution to this work is questionable although their overall

effect is most positive.

I wish to thank many of my colleagues who contributed to the work that is described in this work, and primarily to our group's long-term collaborators Stewart Aitchison and Roberto Morandotti. The spatiotemporal focusing work was an enjoyable collaboration with Shimshon Bar-Ad. I enjoyed and learned from many discussions with Yaron's other students such as Yaniv Bar-Ad and Dvir Yelin. Among the many others who contributed to different phases of this work are Ulf Peschel and Daniel Mandelik. Financial support from the Israeli Ministry of Science and Sports through the Eshkol fellowship helped to fund this work.

Contents

1	Discrete Optics	1
1.1	Introduction	1
1.2	Discrete Diffraction	3
1.3	The Diffraction Relation	4
1.4	Nonlinear Excitations – Discrete Solitons	7
1.5	Dynamics of Light in a Waveguide Array	8
2	Nonlinear Experiments	11
2.1	Experimental Considerations	11
2.2	Experimental Setup	12
2.3	Demonstration of Discrete Solitons	14
2.4	Discrete Solitons from Various Excitations	16
2.5	Studies of Discrete Soliton Dynamics	20
2.6	Self-Defocusing Under Anomalous Diffraction	24
2.7	Interaction with a Linear Defect State	27
3	Linear Effects in Inhomogeneous Arrays	31
3.1	Bloch Oscillations	31
3.2	Anderson Localization	34
3.3	Diffraction Management	37
4	Kerr Spatiotemporal Self-Focusing	43
4.1	Experimental Results	44
4.2	Numerical Model	50
A	Diffraction Curves	53
B	Spatiotemporal BPM Code	59
	Bibliography	63
	Index	68
	Epilog	69

Chapter 1

Discrete Optics

1.1 Introduction

Optics deals with continuous objects. The optical electro-magnetic fields are continuous functions. Optical elements like mirrors and lenses can be presented as continuous operators. Discrete optical fields, which have values only at specific locations, are somewhat unnatural. Nevertheless, there are situations where optical systems can be described by discrete fields. In particular, the interaction of several coupled modes is usually approximated by a discrete set of coupled mode equations [1]. One such case is that of coupled one-dimensional waveguide array [2, 3]. In a waveguide array, large number (infinite in principal) of one-dimensional single-mode waveguides (e.g. optical fibers) are laid one near the other such that their individual modes overlap. The transversal propagating field is now described by an infinite set of complex amplitudes of the individual modes.

The problem of light propagation in an infinite coupled array of waveguides was treated first theoretically by Jones [2], and later demonstrated by Yariv and co-workers [3], who fabricated such an array in GaAs. The nonlinear problem was discussed only years later by Christodoulides and Joseph [4]. They showed that the equations describing propagation in a nonlinear Kerr array are formally a discrete version of the nonlinear Schrödinger equation (NLSE), and that they may have solitary solutions equivalent to the NLSE solitons. The study of the discrete nonlinear Schrödinger equation (DNLSE) became quite popular in the early 90's and many of the properties of discrete solitons were discovered then. Among the topics investigated were instabilities and solitary solutions of discrete structures [5–7], phenomena of steering and switching [8–10], nonlinear dynamics in non-uniform arrays [11–14], temporal effects in discrete solitons [15–18], dark solitary solutions [19, 20], vector discrete solitons [21] and discrete soliton bound states (“twisted modes”) [22, 23].

It should be noted that similar discrete equations appear in other area of physics. In particular, in the context of energy transport in molecular systems

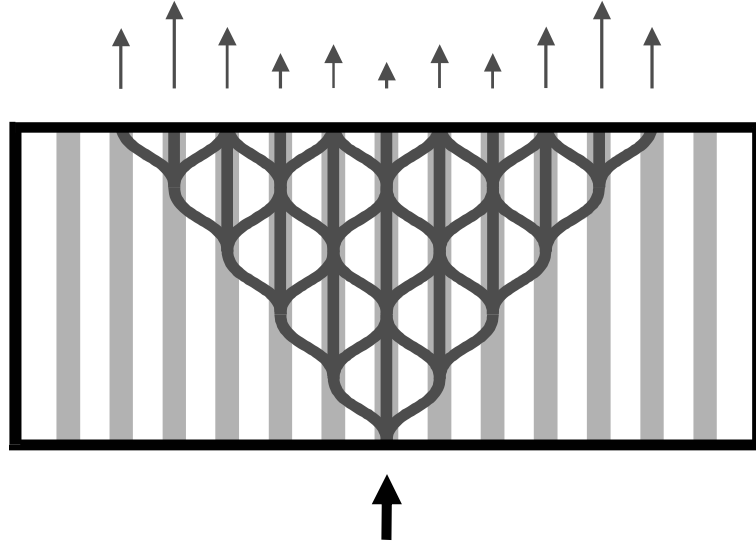


Figure 1.1: A scheme describing light coupling in a waveguide array

[24], localized modes in molecular systems such as long proteins [25], polarons in one dimensional ionic crystals [26], and localized modes of nonlinear mechanical [27] and electrical lattices [28]. The broader area of discrete nonlinear equations and discrete breathers has been reviewed recently [29].

The study of discrete optical solitons has remained primarily a theoretical area until recently, when several experimental studies have been reported by our group. Experiments in GaAs waveguides demonstrated the formation of discrete solitons [30] and later studied many of their properties [12, 31, 32]. These studies led to a renewed interest in the linear properties of discrete optical structures. For example, recent reports on optical realization of Bloch oscillations in waveguide arrays [33–36], and engineering of diffraction using discrete optics [37].

Although we will not discuss any specific applications of the structures or phenomena described here, it is obvious that these waveguide arrays offer several advantages as compared with the more familiar nonlinear slab waveguides. Let us just mention the inherent compatibility with fiber and waveguide devices for input or output, and the possibility to engineer the strength of diffraction for a particular power requirement.

This chapter is organized as follows: we begin by analyzing the basic phenomena that are related to propagation of light in an infinite set of coupled optical waveguides. This broadening of spatial light distributions as a result of discrete diffraction is formulated. We discuss this linear phenomenon first, and

then proceed to discuss nonlinear structures, when discrete diffraction is accompanied by the optical Kerr effect. This combination leads to the formation of discrete solitons and to their dynamic properties. This theoretical section is not exhaustive, and the reader is referred to the bibliographic list for more detailed publications on this topic.

1.2 Discrete Diffraction

Consider an infinite uniform array of identical single mode waveguides. We denote the set of amplitudes of the modes of the individual waveguides as $\{E_n\}$, where n is the waveguide index, $n = 0$ being the central waveguide. The overlap between nearest-neighbors modes has a dominant effect on propagation. It results in a phase sensitive linear coupling between the waveguides, leading to power exchange among them (see Fig. 1.1).

The basic linear set of equations, which describes the light propagation in waveguide arrays using coupled-mode theory formulation is [1]:

$$i \frac{dE_n}{dz} = \beta E_n + C (E_{n-1} + E_{n+1}) . \quad (1.1)$$

z is the spatial coordinate in the direction of propagation, β is the propagation constant of the individual waveguides and C is the coupling coefficient. If only two waveguides are coupled, an arrangement known as an optical directional coupler [1], light is completely transferred from one waveguide to the other after propagating a distance of $z_c = \pi/2C$, the *coupling length*. There is a known mathematical solution for this infinite set of equations [2]. In the case of a unity amplitude single input into the central waveguide and no power in the rest, the electrical field evolution is given by:

$$E_n = (i)^n \mathcal{J}_n(2Cz) , \quad (1.2)$$

where $\mathcal{J}_n(x)$ is the n^{th} order Bessel function. Because the evolution equations are linear, any other solution can be constructed from this solution by a linear superposition. The single input linear evolution is depicted in Fig. 1.2. Notice how most of the light is concentrated in two distinct lobes.

An interesting limit of (1.1) is when the excitation is varying slowly between neighboring waveguides ($E_{n+1} - E_n \ll E_n$) [4,38]. Applying the transformation $E_n = A_n \exp[i(2C + \beta)z]$, we get propagation equations of the form:

$$i \frac{dA_n}{dz} = C (A_{n-1} - 2A_n + A_{n+1}) . \quad (1.3)$$

Changing the discrete coordinate n to a continuous one, $x = nd$ where d is the distance between the centers of two adjacent waveguides, we notice that the right-hand side of (1.3) is a discrete version of a second derivative, hence:

$$i \frac{\partial A}{\partial z} = Cd^2 \frac{\partial^2 A}{\partial x^2} . \quad (1.4)$$

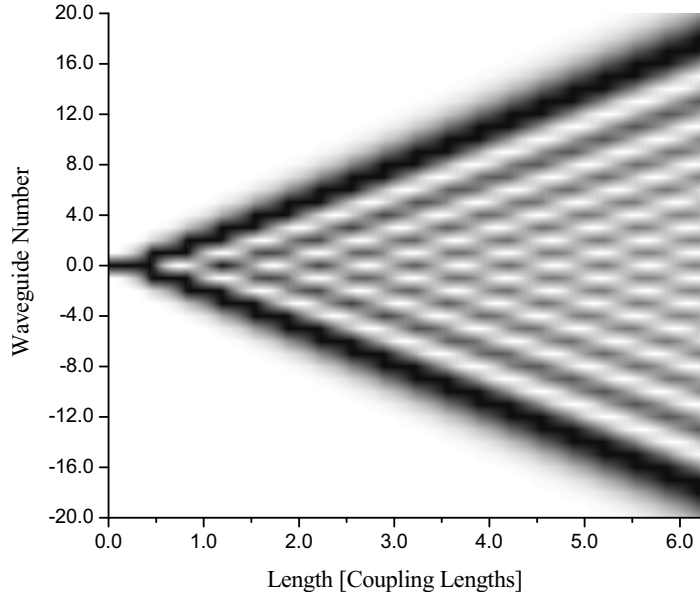


Figure 1.2: Solution for a linearly coupled array of 41 waveguides, when light is injected into the central waveguide, with $E_0 = 1$. The intensity is shown in gray scale. The scale is chosen such that the peak intensity for every propagation distance along the waveguide is represented by black. The energy is spread mainly into two lobes. The number of central peaks is an indication to how many coupling lengths the light has propagated

Equation (1.4) describes, under the assumption of paraxiality, propagation of light in free two-dimensional space. We identify the coupling terms in (1.1) as the cause for *discrete diffraction*. Note, however, that in paraxial diffraction the coefficient of the right-hand side is $1/2k$, with k the wavenumber in the medium. Hence, we see one possible advantage of discrete optics: it enables the engineering of the magnitude of the diffraction, normally fixed at a given wavelength, through the design of the array and the coefficient C . We shall see in the next section even more possibilities for diffraction manipulation.

1.3 The Diffraction Relation

In order to understand diffraction in discrete systems, it is worthwhile to examine first the continuous case. Just as chromatic dispersion results from different phases accumulated by different frequency components, diffraction results from different phases accumulated by the various spatial frequency components [37].

These components are the Fourier components of the beam profile:

$$\tilde{E}(k_x) = \int_{-\infty}^{\infty} E(x) \exp(ik_x x) dx, \quad (1.5)$$

where we define x as the transverse dimension and z as the propagation dimension. The third direction, y , is omitted for simplicity, but can be added in a straightforward manner. Each of the spatial components denoted by k_x is a plane wave [39] which accumulates optical phase differently while propagating. The amount of phase gained by each k_x component after propagating distance z is $\phi(k_x) = k_z(k_x) \cdot z$. A group of transverse components centered at k_x is transversely shifted by an amount of $\Delta x = \frac{\partial \phi}{\partial k_x} = \frac{\partial k_z}{\partial k_x} z$. The beam broadens because of the divergence between the different displacements $\Delta x(k_x)$. The propagation direction in real space of the power contained in each component, the Poynting vector, points perpendicular to the $k_z(k_x)$ curve at k_x [40]. We define the function $k_z(k_x)$ as the *diffraction relation* and the divergence $D = \frac{1}{z} \frac{\partial^2 \phi}{\partial k_x^2} = \frac{\partial^2 k_z}{\partial k_x^2}$ as *diffraction*, in analogy to the definition of dispersion. More about the uses of diffraction relations can be found in appendix A.

The diffraction relation for a specific system can be derived from the evolution equation by assuming a plane wave solution of the form $E(\vec{r}) = E^0 \exp(i\vec{k} \cdot \vec{r})$ where \vec{k} is a vector in spatial frequency space whose components are k_x and k_z . For a scalar propagation in free two-dimensional space, according to the standard time-independent wave equation, the diffraction relation is:

$$k_z(k_x) = \sqrt{k^2 - k_x^2}, \quad (1.6)$$

where $k = \frac{2\pi n_0}{\lambda_0}$ is the wavenumber in the medium and λ_0 is the wavelength in vacuum. The half-circular diffraction relation for forward propagating free space beams is depicted in Fig. 1.3(a). There are a few useful observations that can be made from this graph:

1. A beam can not have propagating components where $k_x > k$. This results in a maximal resolution for a specific wavelength. For example, the minimal spot size of a focused beam.
2. Light can propagate in all π forward angles. For any direction, there is always a point on the diffraction curve, where the Poynting vector is directed along it.
3. The diffraction value around any component of k_x is always negative ($D_{\text{cont}} < 0$). This fact will have important implications for nonlinear evolution.

Let us now consider the diffraction relation for the discrete propagation equation [40, 41]. We apply the same plane wave solution and the result is:

$$k_z(k_x) = \beta + 2C \cos(k_x d). \quad (1.7)$$

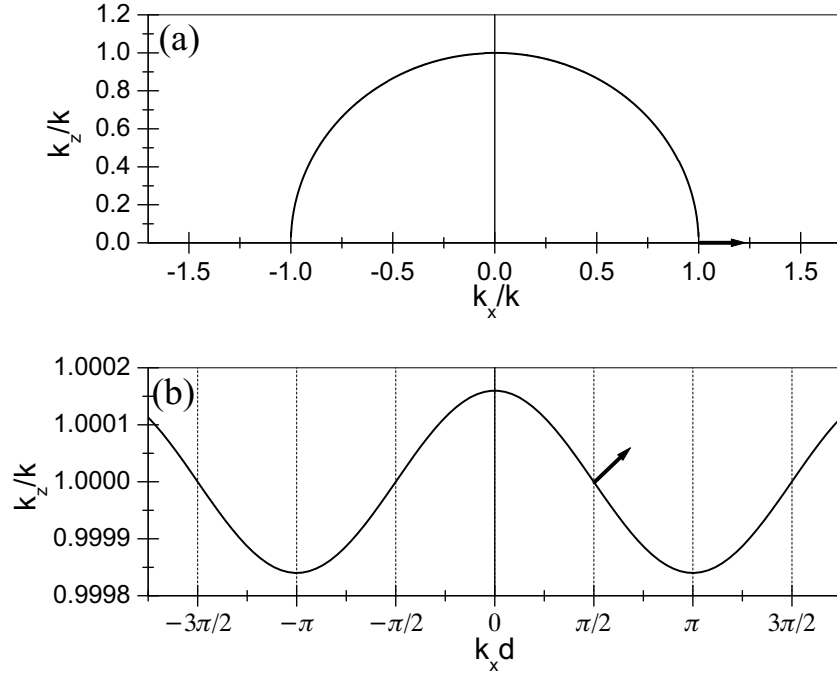


Figure 1.3: Spatial diffraction curves showing phase vs. spatial frequency for (a) continuous and (b) discrete models. The arrows mark the largest possible angle of energy propagation for each model. Only in the discrete case, an inversion of curvature (beyond $k_x d = \pi/2$) leads to anomalous diffraction

The discrete diffraction relation is presented in Fig. 1.3(b). This relation is periodic, hence there are infinite number of components k_x propagating for each k_z , spaced equally by $2\pi/d$. Therefore, we should use a modified function base to span the beam profiles, where each component contains all of these equidistant plane waves. These are the Floquet–Bloch wave functions [42] $E(\vec{r}) = E^0 \sum_{m=-\infty}^{\infty} \Gamma_m \exp \left[i \left(\vec{k} + \frac{2\pi m}{d} \hat{k}_x \right) \cdot \vec{r} \right]$, where Γ_m is a factor related to the individual waveguide mode shape. In a true discrete system, there is only meaning for values of $\vec{r} = (nd, z)$ and Γ_m becomes always unity. We note the similarities between the optical discrete model and the tight binding model of electrons in crystals. The assumption of single-mode waveguide is equivalent to a system of atoms with one S-level electron.

Let us examine the properties of the discrete diffraction curve and its differences from the continuous case:

1. There is a maximal angle of propagation to the z-direction $\alpha_{\max} = 2Cd$.

Even if the input light contains spatial frequencies beyond this angle, they will propagate at a smaller angle.

2. The meaningful range of k_x is $2\pi/d$. Beyond this range, i.e. the first Brillouin zone, any k_x has an equivalent value that is inside it, sharing the same Floquet–Bloch wave function. It is convenient to choose $-\pi/d < k_x < \pi/d$.
3. The curvature of the discrete diffraction curve, or the diffraction value, is negative for $|k_x| < \pi/2d$, zero for $|k_x| = \pi/2d$ and positive for $\pi/2d < |k_x| < \pi/d$. This is in contrast with the continuous case, where zero and positive values of diffraction are impossible. We define the regime of positive diffraction as the anomalous diffraction regime.
4. The diffraction curve has a maximum value as well as a minimum, while the continuous relation has no minimum.

1.4 Nonlinear Excitations – Discrete Solitons

Consider now propagation of light in a Kerr-like nonlinear waveguide array. The Kerr effect is the linear dependency of the refractive index on the local light intensity in a dielectric material [1]. The refractive index varies as $n = n_0 + n_2 I$ where n_0 is the refractive index at low intensities, I is the light intensity and n_2 is the material nonlinear parameter, proportional to the nonlinear electrical susceptibility term $\chi^{(3)}$.

Equation (1.1) is now modified to be [4]:

$$i \frac{dE_n}{dz} = \beta E_n + C (E_{n-1} + E_{n+1}) + \gamma |E_n|^2 E_n , \quad (1.8)$$

where $\gamma = \frac{k_0 n_2}{A_{\text{eff}}}$ and A_{eff} is the common effective area of the waveguide modes. This equation is known as the Discrete Nonlinear Schrödinger Equation (DNLSE). The Kerr nonlinearity in the presence of continuous diffraction (or dispersion) may lead to the formation of spatial (or temporal) solitons [43–46]. These are stable light beams (or pulses), propagating without diffraction (or dispersion). Unlike its continuous counterpart, the DNLSE is not integrable, and therefore it does not possess exact soliton solutions. However, numerical and analytic studies show that it does have solitary-wave solutions that propagate without diffraction. In particular, for a wide excitation, one can use the analogy with the continuous case to derive an approximate shape distribution [4]:

$$E_n(z) = A_0 \exp [i (2C + \beta) z] / \cosh (nd/w_0) , \quad (1.9)$$

where w_0 is the width constant of the light distribution, assumed to be much larger than d . The amplitude is given by $A_0 = \sqrt{\frac{2Cd^2}{\gamma w_0^2}}$. Narrow solitary wave solutions are also possible, but they deviate from this shape function. It is quite

obvious that at very high powers, all the light is concentrated in a single waveguide, increasing its index of refraction so that it is completely decoupled from its neighbors. Although, formally speaking, all of these solutions are solitary waves, we shall use the term *discrete solitons* to describe all nonlinear non-diffracting waves.

Before we move to discuss other properties of discrete solitons, it is worthwhile to discuss how one may infer their existence from the diffraction relations. The effect of the Kerr nonlinearity on the diffraction relations is similar for continuous and discrete cases. These relations are, respectively:

$$k_z(k_x) = \sqrt{k^2 \left[1 + \left(\frac{n_2 I_0}{n_0} \right)^2 \right]} - k_x^2, \quad (1.10a)$$

$$k_z(k_x) = \beta + 2C \cos(k_x d) + \gamma I_0. \quad (1.10b)$$

Here I_0 is a measure of the optical power contained in the beam and it is proportional to $|E^0|^2$. In both cases the light intensity shifts the excited modes upward along the k_z axis.

There is a useful phenomenological way of understanding paraxial solitary waves [29]. As discussed above, diffraction results from the curvature of the diffraction relation. In the presence of significant nonlinear Kerr effect the wave increases its effective propagation constant, and, eventually, shifts it out of the diffraction zone, eliminating the option for beam broadening. For diffraction to happen, the beam spatial components have to be able to radiate along the \hat{x} -axis. When they are outside the linear spectrum, this radiation is eliminated. It is now clear that in continuous homogeneous media, where the diffraction curve has a maximum, bright solitons are possible only when $n_2 > 0$. Negative values of n_2 will only lower the value of the propagating k_z frequencies, and actually enhance the rate of diffraction.

In contrast, the discrete diffraction curve has both negative and positive curvatures, which enable the formation of bright discrete solitons for both positive and negative n_2 [4, 6, 29, 30, 32, 47, 48]. Furthermore, this curve is limited both from top and bottom to the range $\{\beta - 2C < k_z < \beta + 2C\}$ resulting in more options for solitary waves. For example, in a positive n_2 material, an excitation experiencing positive curvature at the optical band bottom, and therefore nonlinear defocusing, can still be solitary if enough power is supplied such that it is pushed upward enough so it emerges out of the optical band. In fact, any excitation in any type of material will be eventually solitary in the discrete optics case because of the bounded band.

1.5 Dynamics of Light in a Waveguide Array

When we consider the dynamics of light in a waveguide array, it is important to understand the direction of energy flow. It is easy to show that in the two waveguides coupler the phase relation between the two individual modes is always $\pm\pi/2$ and that power is always flowing from the mode, whose phase

is retarded relative to the other. Similarly, from the linear solution for the propagation of a single waveguide input, we find that the same phase relation between waveguides of $\pm\pi/2$ occurs in an infinite waveguide array. At the outer regimes of the diffracting light, power transfer is outwards, while in the center, a more complex phase structure evolves. For different input conditions this phase structure disappears, but power still flows out from waveguides, which their phase is retarded relative to their neighbors.

This is not the case for discrete solitons. By definition, the phase across a soliton is flat. A flat phase front results in no power coupling, therefore no diffraction, exactly what we expect from a soliton. The Kerr effect is the cause of this flatness, by increasing the refractive index of some waveguides, hence accelerating their phase evolution.

Continuous solitons possess two fundamental geometrical symmetries of space. Under rotations of the axes and translation of their origin, exactly the same mathematical solution is reproduced. On the other hand, for discrete optics both symmetries are broken due to the direction and position of the array waveguides [7]. Rotational symmetry is gone all together while translational symmetry is reduced. There is still option to translate solutions to other z values, while in the x direction only a discrete translational symmetry is left because of the periodicity d in that direction. Nevertheless, discrete solitons can be centered either on a waveguide or exactly in between two adjacent waveguides [6]. Even more, solutions of discrete solitons that propagate with an angle to the \hat{z} -axis do exist [8–10]. The discrete nature though, is still reflected in some new discreteness-induced effects [31].

In order to learn about the effect of launching discrete solitons centered at different lateral positions, we look at the generalized Hamiltonian of (1.8):

$$H_{\text{disc}} = \sum_n \left[C |E_n - E_{n-1}|^2 - \frac{\gamma}{2} |E_n|^4 \right]. \quad (1.11)$$

The first term is a generalized kinetic energy term and the second is an interaction energy term. Plotting H_{disc} as a function of the lateral center of the soliton beam shows an oscillating function. The Hamiltonian minima are when the soliton center is on a waveguide site and its maxima are when the soliton is centered between two adjacent waveguides. This discreteness induced periodic potential is known from solid state physics as the Peierls–Nabarro (PN) potential [7]. It is a result of the combination of nonlinearity and discreteness. The depth between the minima and maxima points is power dependent. Solitons experiencing this potential will be stable for small lateral shift when centered on a site and unstable if centered in between two sites.

If a discrete soliton which is wider than one waveguide is excited, it can be forced to hop sideways while propagating in the z direction [8–10]. A linear phase gradient across its profile such as $\phi_n = n\Delta\phi$ will allow the light distribution to keep its solitary properties, but the soliton will also move away from the retarded phase side. This is understood when examining the direction of energy flow. However, increasing the power of the excitation leads to a new, discreteness

induced effect. At high power the waveguides that contain light are decoupled from their neighborhood. Therefore, a discrete soliton will be locked at high powers to its input waveguides and will not travel sideways anymore [9, 10, 31]. The power dependence of the propagation angle is called discrete soliton *power steering*. It can be also thought of as interplay between the PN potential and the generalized kinetic energy of the soliton.

Chapter 2

Nonlinear Experiments in Waveguide Arrays

While many have contributed to the theoretical understanding of discrete solitons, the experimental studies have been carried out primarily at our group at the Weizmann Institute, in close collaboration with the Aitchison group at the University of Glasgow. In the following chapter we shall review these results.

2.1 Experimental Considerations

Two ways were proposed in the past for realizing an optical discrete system. One is to form the array by patterning a slab planar waveguide [2,3]. The other is a multi-core optical fiber where the cores are arranged in a circular shape [8,49]. There are a few advantages for each of the configurations. Slab waveguides can be made from a variety of materials while optical fibers are typically made of glass variants. There are many standard techniques for patterning planar configurations, while multi-core fibers are not so common and easy to make. Integrating arrays with other elements is easier on a planar layout. On the other hand, very long fibers can be formed compared to only a few centimeters of planar waveguides. The periodic boundary conditions that are achieved with the circular layout of multi-core fibers are very attractive as it can better simulate an infinite array.

In our experiments, we chose to work with waveguide arrays that were etched of a planar slab waveguide made of AlGaAs [50]. There are a few reasons for this choice. AlGaAs is an effective nonlinear material, about 500 times more nonlinear than fused silica glass [51]. This enables us to use short waveguides, a few millimeters long, and modest optical powers. Working at the communication standard wavelength of $1.5\ \mu\text{m}$, we are below the half of the band gap. Thus, not only linear absorption is minimized but nonlinear two-photon absorption as well. The technology for fabricating AlGaAs waveguides is quite advanced and waveguides of relatively low loss are possible.

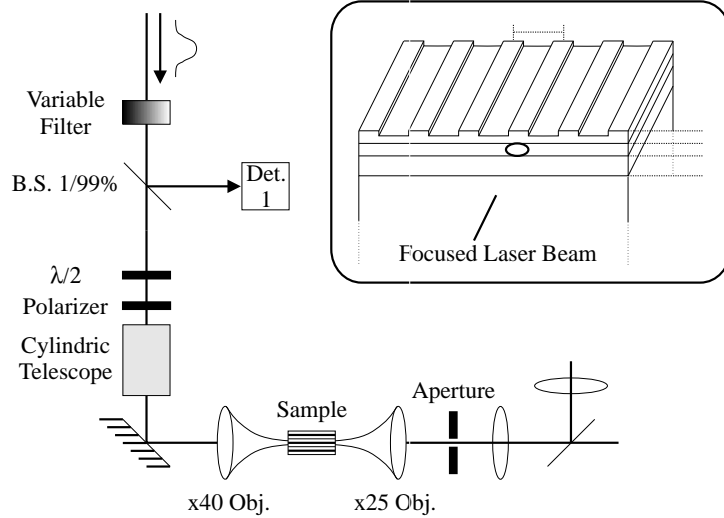


Figure 2.1: The experimental setup. **Inset:** Schematic drawing of the sample. The sample consists of a $\text{Al}_{0.18}\text{Ga}_{0.82}\text{As}$ core layer and $\text{Al}_{0.24}\text{Ga}_{0.76}\text{As}$ cladding layers grown on top of a GaAs substrate. A few samples were tested with different separations d between the waveguides centers

There are some details we should be aware of, though. Coupling light into AlGaAs is relatively ineffective due to its high linear refractive index. With index of 3.3, almost 30 percents are reflected back at the input facet. Normal dispersion is also a factor, broadening an initial pulse of about 100 fs after propagating a typical sample length of 6 mm by about a factor of two. At the highest peak intensities of our experiments, three-photon absorption starts to play a role as well.

2.2 Experimental Setup

We shall review now experiments performed in our group which demonstrate some of the properties of discrete solitons. Our light source was a commercial optical parametric oscillator (Spectra-Physics *OPAL*), pumped by a 810 nm Ti:Sapphire (*Tsunami*). 4 nJ pulses were produced at a repetition rate of 80 MHz. Their average power is 300 mW while each has a peak power of about 40 kW. The pulse length is about 100 fs and the wavelength is tunable between 1450 nm to 1570 nm. We usually worked at a wavelength of 1530 nm in order to minimize both two- and three-photon absorption.

The AlGaAs waveguides are patterned by either photolithography or electron-beam lithography. The core-clad index difference is achieved by different Aluminum concentration. The waveguides are typically 4 μm wide and

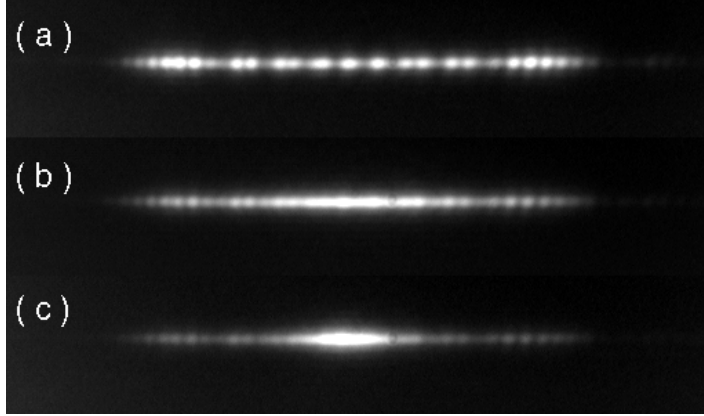


Figure 2.2: Images of the output facet of a sample with $d=8\mu\text{m}$ for different powers. (a) Peak power 70 W. Linear features are demonstrated: Two main lobes and a few secondary peaks in between. (b) Peak power 320 W. Intermediate power, the distribution is narrowing. (c) Peak power 500 W. A discrete soliton is formed

6 mm long. The separation between waveguide centers is varied from $8\mu\text{m}$ to $11\mu\text{m}$ in order to have samples of different coupling lengths. The larger the distance the smaller the coupling. The individual waveguide mode shapes are somewhat oval. Arrays of 41 and 61 identical waveguides were made, in order that the light will experience an effective infinite system and will not reach the array borders.

The experimental system is described in (Fig. 2.1); the power of the input is tuned using a variable filter. A beam sampler picks up a small part of the power to an input power detector. The beam is shaped into an oval shape through cylindrical optics in order to match the individual waveguide mode or, alternatively, into a wider beam if input into a few waveguides is needed. The light is coupled into the sample through a $40\times$ input objective. A glass window, 1 mm thick, is inserted in front of the input objective. By rotating this window, small parallel translations of the beam are transformed by the objective to small variation in the angle of incidence at the focal plane, enabling a phase gradient across the beam. After propagating along the sample, the light is collected from the output facet by a second objective. A second beam splitter is sending some of the power to an output power detector. The output objective and another lens image the light from the output facet onto an IR sensitive camera. At the extra focal plane which is formed between the objective and the lens, a slit can be inserted in order to sample different parts of the image for spectra and auto-correlation measurements. Finally, a computer captures the camera image and the other data for further analysis.

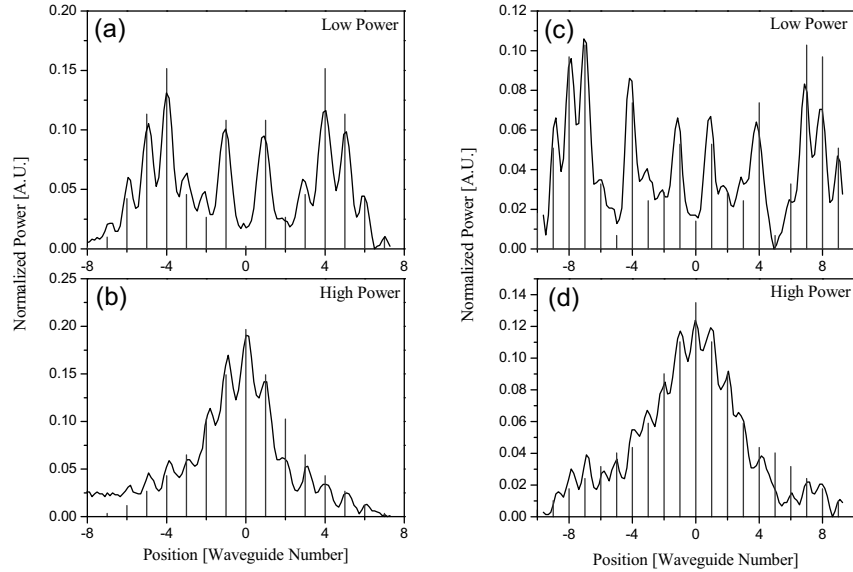


Figure 2.3: Single waveguide excitation: Experimental and numerical results for samples with $d=11\ \mu\text{m}$, total propagation distance of 1.9 coupling lengths (a,b) and $9\ \mu\text{m}$, total propagation distance of 3.0 coupling lengths (c,d). Both experimental results (solid line) and numerical results (vertical lines) are shown. The integrated power is normalized to unity

2.3 Demonstration of Discrete Solitons

We first describe the basic experiments for the observation of discrete solitons [30]. We used a 6 mm long sample of 41 waveguides. Light was injected into a single central waveguide, as was described before. The first observation is presented in Fig. 2.2 as the output facet images that were captured by the camera. At low power, a wide distribution is obtained, covering about 35 waveguides. This distribution matches what is expected from a 4.2 coupling-lengths long sample (see Fig. 1.2). When the power is increased, we first see the light distribution converging to form a bell-shape. Launching even more power leads to the formation of a confined distribution around the input waveguide, a discrete soliton.

Transverse cross-sections of the output profile for two samples of different coupling lengths are compared in Fig. 2.3. Figures 2.3(a,b) are from a 1.9 coupling lengths long sample at low and high powers, respectively. Figures 2.3(c,d) are from a 3.0 coupling lengths long sample at low and high powers, respectively. The difference in the coupling length is obtained by varying the distance d between adjacent waveguides in the two samples (from $11\ \mu\text{m}$ to $9\ \mu\text{m}$). The solid curves correspond to the experimentally measured profiles, while the height

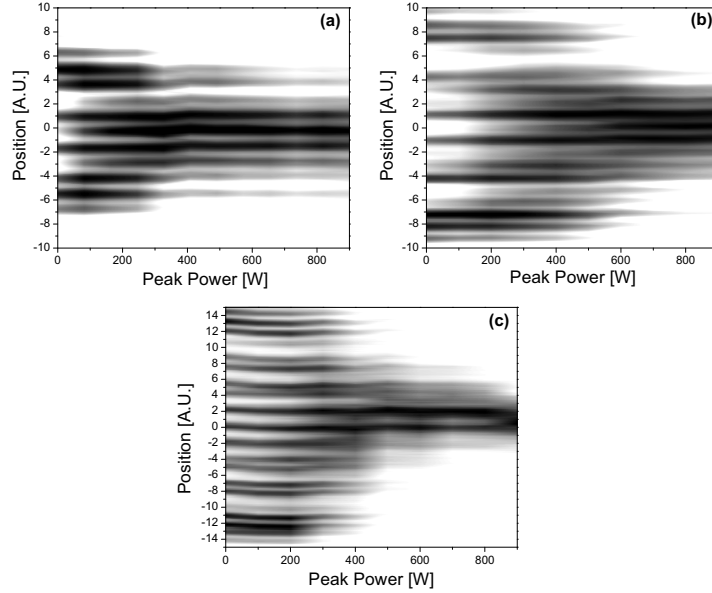


Figure 2.4: Single waveguide excitation: Output light distributions as a function of the input peak power. Vertical cross-sections are the different power profiles corresponding to each input power. The three frames (a–c) are taken from samples of 1.9, 3.0 and 4.2 coupling lengths, respectively

of the vertical lines stands for the light intensity in each respective waveguide according to a numerical solution of Eqs. 1.8. The agreement between the experiment and the numerical solution is good, both at low and at high powers. At low power, most of the light energy is pushed out to the profile wings, while characteristic secondary narrow peaks appear in between. The number of these secondary peaks is an indicator to the amount of coupling lengths propagated. When the power is increased (estimated to about 900 W at peak power), light is confined to the vicinity of the central input waveguide.

It is interesting to check the power dependency of the visibility between adjacent peaks in Figs. 2.2 and 2.3. We define the visibility of the n^{th} mode as a function of the intensity values $I(x) = |E(x)|^2$ at the center of two waveguide modes and the intensity value in between them:

$$V_n = 1 - \frac{2I[(n + \frac{1}{2})d]}{I[nd] + I[(n + 1)d]} . \quad (2.1)$$

The mode visibility has a minimal value when the light is in-phase between waveguides n and $n + 1$. It is maximal when the light is completely out-of-phase and the intensity is equal in both waveguides. Checking the experimental results of Figs. 2.2 and 2.3 we observe a visibility of about half for all the linear

cases. This is in a good agreement with the $\pi/2$ phase relation predicted by the solution of Eqs. 1.8. The visibility is degraded because of launching light distribution that does not match exactly the central waveguide mode and due to cross-talk between the pixels of the IR camera. When the power is increased, the soliton formation forces a smoother phase relation between light in neighboring waveguides and the mode visibility decreases.

In order to demonstrate a power stability regime of the discrete soliton, we present in Fig. 2.4(a-c) power evolutions of the output profiles for the two cases of Figs. 2.3 and for the case of Fig. 2.2. Each vertical slice is a power cross-section at a respective power. At low power, the light distribution is broad and most of the light is far from the input waveguide. As the power is increased, light is gradually confined to the center. The important fact to note is that after achieving a certain distribution width, the focusing process almost arrests, and only a slight variation of the width with power is observed. It occurs at about 600 W for all the samples.

2.4 Formation of Discrete Solitons from Various Excitations

Until now, we only described discrete solitons that were formed by launching light into a single waveguide. This is equivalent to exciting uniformly all available spatial frequencies, because a single waveguide represents a discrete δ -function excitation. The single waveguide excitation is the case where the discrete nature of the waveguide array is most pronounced. As can be seen in Fig. 1.3, the continuous and discrete diffraction curves have the same curvature for small spatial frequencies. Only when high enough frequencies are excited in the array, discreteness can be pronounced.

Solitons are not affected by such considerations. They are formed in a continuous slab waveguide as well as in an array, as long as enough power is supplied. We present here the results for excitation with various beam widths and shapes. As the launched beam becomes wider and smoother, the narrower is the excited spatial frequency range and the beam experiences diffraction to a smaller extent.

To launch wide input fields, we used arrays with power splitters as input channels. The power splitters were multiple Y-junctions, which split the launched power from one waveguide, almost equally into several waveguides. The output of the splitter was injected into the waveguide array such that each splitter branch is coupled into one waveguide. As a result, the launched light distribution is a discrete rectangular function. It is narrower in its frequency content, but due to the sharp distribution edges, it still contains all of the high spatial frequencies.

Figure 2.5 presents the results for low and high power when the power was split into three and five waveguides. The output profiles for a three waveguides input are plotted on Figs. 2.5(a,b) and for five on Figs. 2.5(c,d). The array spacing is $9\mu\text{m}$ for both samples, which results in 3.0 coupling-lengths

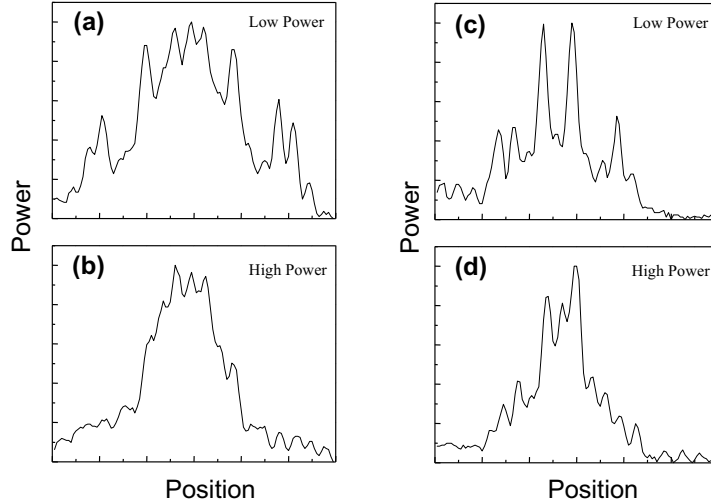


Figure 2.5: Wide excitation by power splitting: Output profiles, as seen on the IR camera, of three waveguides wide (a,b) and five waveguides wide (c,d) excitations. All the samples are of 3.0 coupling lengths

propagation. In the linear low power cases, we see less expansion than in the single waveguide input case due to reduced diffraction of the light. In the single input case the light occupied about 20 waveguides after propagating through the sample, while for the three and five waveguides excitation, it expands only to about 17 and 11 waveguides, respectively. For low power, we still see the character of discreteness: some power concentration at the edges and a peaky nature at its center due to out-of-phase relations between the light in neighboring waveguides. Increasing the power causes both distributions to become somewhat narrower. There is a strong effect on the waveguide phases. They are locked together by the nonlinearity as a discrete soliton is formed, and the mode visibility is degraded.

It is also possible to launch a broad light distribution without any sharp features to avoid excitation of high spatial frequencies. These distributions extent over a limited range of frequencies are associated with a limited excitation around the center of the diffraction curve, and therefore should behave much like in a continuous system. We inject the light directly into the array after shaping the input beam into a wide ellipse by cylindrical optics. The beam overlaps a few waveguides and the relative power in each of them varies smoothly according to the beam gaussian profile. The results of two such experiments are presented in Fig. 2.6. Beams covering about two and three waveguides were tested and their output profiles as a function of input power are shown in Figs. 2.6(a) and 2.6(b), respectively. As before, we observe the formation of discrete solitons. However, they now behave more like regular continuous solitons as their profile

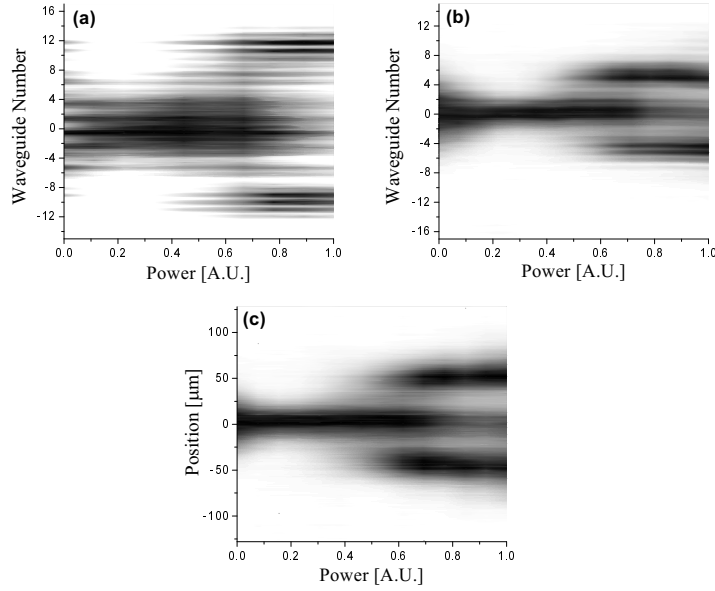


Figure 2.6: Wide excitation by a wide smooth beam: Output light distributions as a function of the input peak power as in Fig. 2.3. (a) A two waveguides wide excitation. (b) A three waveguides wide excitation. (c) A three waveguides wide excitation of a continuous slab waveguide

is bell-shaped and only their width is changing as the power is increased. As with continuous one-dimensional solitons, less power is required to form a wider soliton, therefore the minimal width is reached for weaker intensities than in the single waveguide input case.

Wide discrete solitons exhibit an interesting effect at a power of twice their formation power. Instead of just becoming narrower, when there is enough power for the formation of two solitary beams, the discrete soliton breaks into two. This result has been explained for the continuous case as an instability of the second soliton [52]. The cause for this instability in our case is probably a perturbation to the soliton shape by two- and three-photon absorption. The splitting of a three waveguides wide discrete soliton and of a continuous soliton of a similar width in a planar slab waveguide are compared in Figs. 2.6(b) and 2.6(c), respectively. The two cases are clearly very similar, and a three waveguides excitation is almost indistinguishable from a continuous soliton. Recall that a single waveguide excites all the frequencies of the Brillouin zone (see Fig. 1.3(b)), between $-\pi$ and π , while a two waveguides wide input would excite only half of this range ($-\pi/2$ to $\pi/2$) which has only one curvature sign. It is not surprising then that by launching a light distribution which is three waveguides wide ($-\pi/3$ to $\pi/3$), even less spectrum is generated, hence the behavior is very

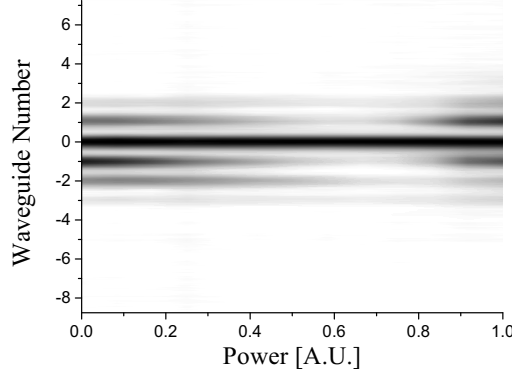


Figure 2.7: Nonlinear contraction of power into a single waveguide

similar to continuum.

Using specific conditions of wide excitation and very weak coupling between the waveguides, we achieved contraction of most of the light into a single central waveguide. The output distribution as a function of input power is depicted in Fig. 2.7. By increasing the power, the distribution narrows until all the light is concentrated in a single waveguide. By further increasing the power, the light couples again into more waveguides. This is explained by nonlinear two-photon attenuation and self-phase modulation induced broadening, which are enhanced at the large intensities that are obtained when all the power is concentrated in one waveguide.

In all of the experiments described above, the main reason for differences between the results and the predictions of simple coupled-mode theory (CMT) [1] is the temporal evolution of the pulsed input field [15,17]. In order to examine the pulse effects on the results, we recorded temporal auto-correlation traces of a discrete soliton. A slit was used to select light from the soliton center or from its wing, a few waveguides away from the input center. A comparison between the two results, together with the input pulse auto-correlation are shown in Fig. 2.8(a). The pulse length at the soliton center is doubled due to the normal dispersion of AlGaAs and the nonlinear effect of Self-Phase Modulation (SPM) [53]. At the soliton wing, there is an evidence for temporal splitting. The reason for this splitting is the depletion of light from the wings when the stronger spatial focusing occurred near the peak of the pulse. To illustrate this pulse shape, we draw a top view of the pulse in Fig. 2.8(b). The spectral broadening of the pulse center is a measurement for the importance of SPM on the temporal evolution. In Fig. 2.8(c) the spectra of the input pulse and the output pulse center are compared. The difference in widths is clear and we can estimate from the oscillatory profile of the output spectrum that SPM introduced a nonlinear phase shift of about $3\pi/2$.

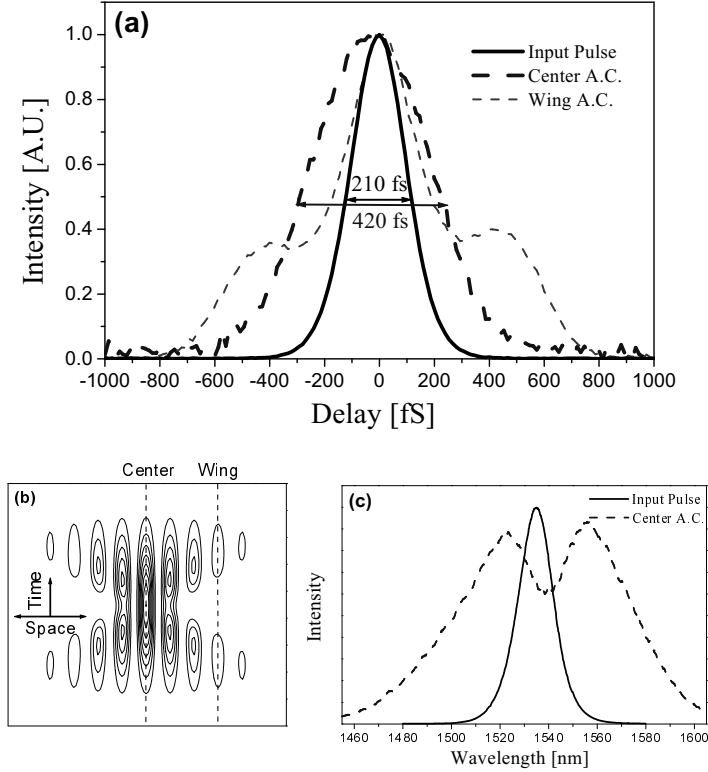


Figure 2.8: **(a)** Temporal auto-correlation of a discrete soliton: the input pulse (*solid line*), the output pulse center (*thick dashed line*) and the output pulse wing (*thin dashed line*). **(b)** The output pulse sketch. **(c)** A comparison between the spectra of the input (*solid line*) and the output (*dashed line*) pulses

2.5 Studies of Discrete Soliton Dynamics

We divide the experiments involving dynamics of discrete solitons in waveguide arrays into two categories [31]. In one type of experiments, a phase gradient is applied along the profile of the input beam, thus giving it transverse kinetic energy (the first term in (1.11)) and forcing the soliton to move across the array. In the other kind of experiments, the beam is launched along the waveguide direction while its input position is scanned in between two adjacent waveguides. The experiments of the first category examine the rotational symmetry breaking in discrete systems, while those of the second category investigate the translational symmetry breaking.

We recorded the output light distribution for various input angles at the power required for launching a soliton. Rotating a glass window positioned

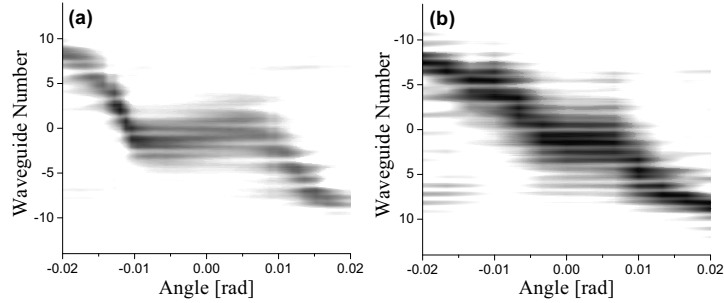


Figure 2.9: Discrete soliton power steering: Output light distributions as a function of the input angle of (a) two and (b) three waveguides wide initial beams. In the two waveguides wide case, the locking for angles smaller than 0.01 radian is very clear

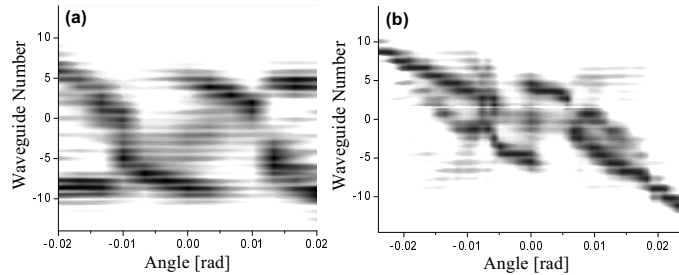


Figure 2.10: Repeating the experiments of Fig. 2.9 for a two-soliton excitation. The symmetry of the soliton splitting is broken

in front of the input objective controls the input angle. The results for two- and three-waveguides wide excitations are presented in Figs. 2.9(a) and 2.9(b), respectively. Imposing a phase gradient across a single waveguide input has no meaning because phase difference between different waveguides is required for beam steering. Hence a beam coupled to a single guide always move along the waveguides. In the other extreme, the continuous case of a slab waveguide, we expect the output center to move linearly with input angle changes. In the intermediate cases of discrete solitons that extends over a few guides, power dependent locking [9] is expected due to the PN potential [7]. In Fig. 2.9(a) we note that although small angles are imposed on the input beam, its output center position does not change. Only beyond a critical angle where the kinetic energy overcomes the PN energy barrier, the soliton starts to move across the array. As the input beam becomes broader, the shallower PN potential allows the escape of the discrete soliton at a smaller angle. The smaller locking region

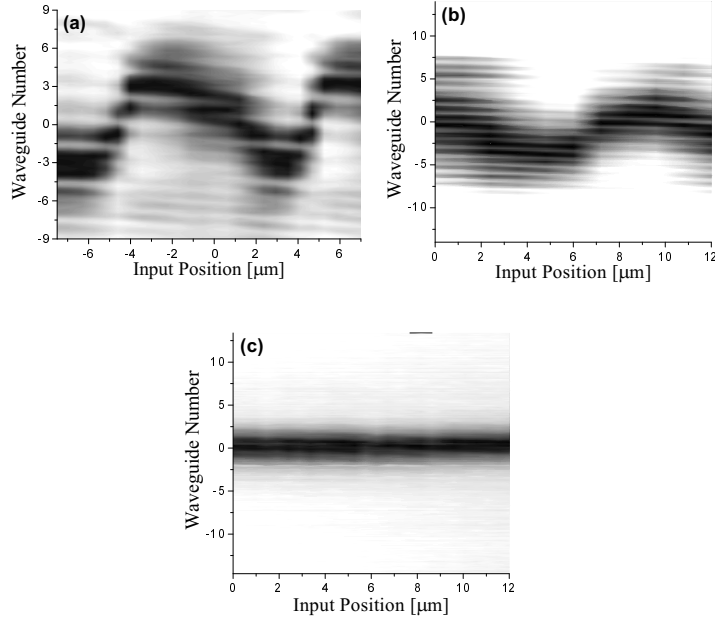


Figure 2.11: Discrete soliton translation induced steering: (a–c) Output light distributions as a function of the input position for one, two and three waveguide excitation, respectively. Amplified oscillations of the output position are observed. The oscillations are clearly induced by discreteness as they disappear as the excitation becomes wider

in Fig. 2.9(b) compared to Fig. 2.9(a) demonstrates this effect.

An interesting result was obtained when the last experiment was repeated with input power which was enough for a second soliton. At a zero angle, the soliton brakes into two, as was shown in Figs. 2.6(a–c). When a tilt is introduced, symmetry is broken and more power goes to one of the two parts. The transition of power between the two parts for a two waveguides wide excitation is clearly seen in Fig. 2.10(a). In the case of a wider three waveguides beam (Fig. 2.10(b)), the splitting is even suppressed at large tilts. A single soliton is formed and its center depends linearly on the input angle.

Results from experiments of the second kind, with beams with flat phase fronts, are presented in Figs. 2.11 and 2.12. In these experiments the beam is launched along the waveguides direction while its input position is scanned transversally across the array. The sample is positioned on top of a piezo-driven stage and by changing the voltage on the piezo-electric element from zero to 1000 V, the sample is shifted by 12 μm. First, the power was fixed such that a single soliton has been formed. Output profiles for three different input widths of one, two and three waveguides are shown in Figs. 2.11(a–c), respectively. We

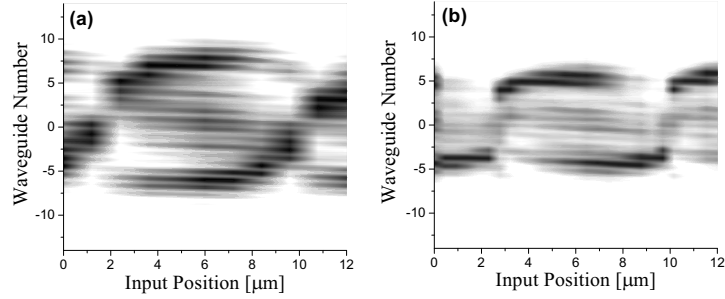


Figure 2.12: Repeating the experiments of Fig. 2.11 for a two-soliton excitation power. (a,b) Results for inputs of two and three waveguides width, respectively. The symmetry of the soliton splitting is broken

observed an amplification of the lateral translation of the beam, which is induced by discreteness. The nonlinear beam is interacting with the PN potential and as a result it is deflected into large angles. The deflection angle passes zero when the beam is centered on a waveguide (position zero in Fig. 2.11(a)) and exactly in the middle between two waveguides at $\pm 4.5 \mu\text{m}$, as can be expected from symmetry reasons. These two states correspond to the two extrema of the PN potential. In all other input positions, a non-uniform division of the power between two waveguides occurs. After a short propagation distance, the waveguide containing more power acquires more phase shift than the other one. The nonlinearly induced phase difference between the two waveguides causes propagation in an angle towards the waveguide containing more light, as we demonstrated before when we tilted the beam deliberately. The difference between the stable minima and the unstable maxima of the PN potential is manifested in the fast crossing of the output distribution at $\pm 4.5 \mu\text{m}$ compared to the slow crossing around zero translation. For wider beams, the PN potential is shallower and the effect is reduced. The effect of a two waveguides wide input is small (Fig. 2.11(b)) while there is none for the three waveguides wide input (Fig. 2.11(c)).

The effect of input translation on the case where there is enough power for two-solitons is similar to the effect of input rotation. As before, symmetry between the two parts of the beam is broken. Translation has a periodic effect because of the periodicity of the array. Therefore, light is repeatedly concentrating into one beam part and then into the other. Figures 2.12(a,b) present these results for the two and three waveguides wide inputs, respectively.

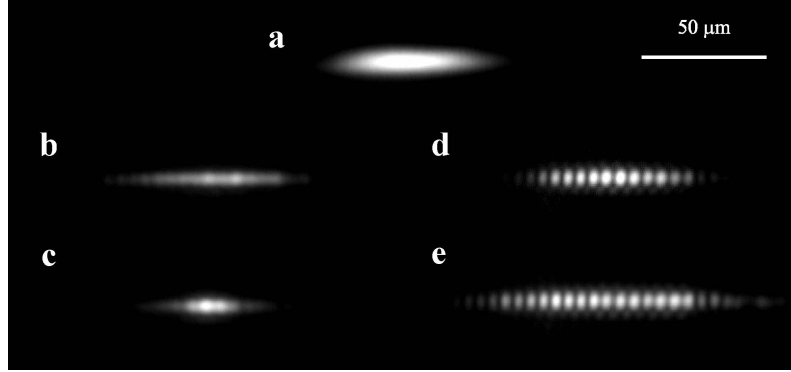


Figure 2.13: Experimental results showing both nonlinear self-focusing and self-defocusing in an array of waveguides, for slightly different initial conditions. (a) The input beam, $\sim 35 \mu\text{m}$ wide at FWHM. (b) Light distribution at the output facet for normal diffraction in the linear regime. The beam slightly broadens through discrete diffraction. (c) At high power ($I_{\text{peak}} \sim 150 \text{ W}$), the field shrinks and evolves into a discrete bright soliton. (d) For an anomalous diffraction condition, when the beam is injected at an angle of $2.6 \pm 0.4^\circ$ inside the array, it broadens slightly as in (b). Note the dark lines between the optical modes resulting from the π -phase flips between adjacent waveguides. (e) When the power is increased ($I_{\text{peak}} \sim 100 \text{ W}$), the distribution broadens significantly due to self-defocusing

2.6 Self-Defocusing Under Anomalous Diffraction

The relation between the nonlinear effects and the diffraction properties was discussed above. For self-focusing to occur in a positive n_2 medium, a negative curvature, i.e. normal diffraction, is required. In the case of discrete diffraction, where the diffraction sign can be inverted, we expect a richer spectrum of nonlinear effects. In particular, at the bottom of the diffraction curve, where the diffraction sign is inverted, as the input beam intensity is increased, the excited k_x modes are pushed up into the spectral band, resulting in a stronger broadening of the beam. This effect, called self-defocusing, could be otherwise observed only in negative n_2 material with slow nonlinear response [6].

Applying tilts to the input beam launches different groups of k_x modes. Because of the high refractive index of AlGaAs ($n_0 \approx 3.3$) the angle inside the slab waveguide is much smaller than in air. The actual angle of energy propagation inside the array may still be different, determined by the slope of the discrete diffraction relation [32]. Thus, for a beam around $k_x = \pi/d$ energy is propagating with a zero angle to the waveguides, just like for $k_x = 0$.

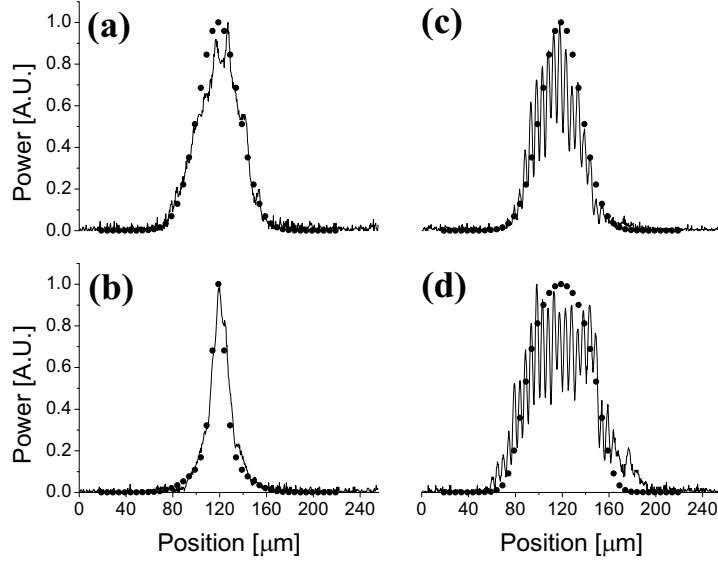


Figure 2.14: Comparison between cross-sections of the experimental results of Fig. 2.13 (*solid line*) and numerical solutions of coupled mode theory (*solid circles*, each represents the power in a single waveguide). (**a,b**) Normal discrete diffraction condition, low and high power, respectively. (**c,d**) Anomalous diffraction condition, low and high power, respectively. Note the difference between nonlinear focusing (**b**) and defocusing (**d**)

Results for beams that were launched at angles corresponding to these two cases are presented in Fig. 2.13. Figure 2.13(a) shows an image of the input beam. Figures 2.13(b,c) are images of the output facet when $k_x = 0$ for low and high input powers, respectively. As can be seen, in this condition of normal diffraction, self-focusing which leads to the formation of bright solitons occurs. Figures 2.13(d,e) are again for low and high power, but when $k_x = \pi/d$ and the diffraction is anomalous. The maximal mode visibility in this case is an indication for the π phase jumps between adjacent guides. When low optical power is injected, the beam is slightly broadened to the same extent as in the normal case. The difference is obvious when the power is increased. Instead of focusing, which is expected in such positive n_2 material, the light distribution expands considerably. Cross-sections of the results are compared to a numerical integration of Eqs. 1.8 (see Fig. 2.14). The experimental results prove to be in a very good agreement with this simple theory.

In the anomalous diffraction regime we should expect to observe dark solitons. A dark soliton is a constant illumination in space, with a central dark notch which is a result of a π phase flip [54]. At low powers, the dark zone broadens due to diffraction. If the right conditions are fulfilled, a stable dark

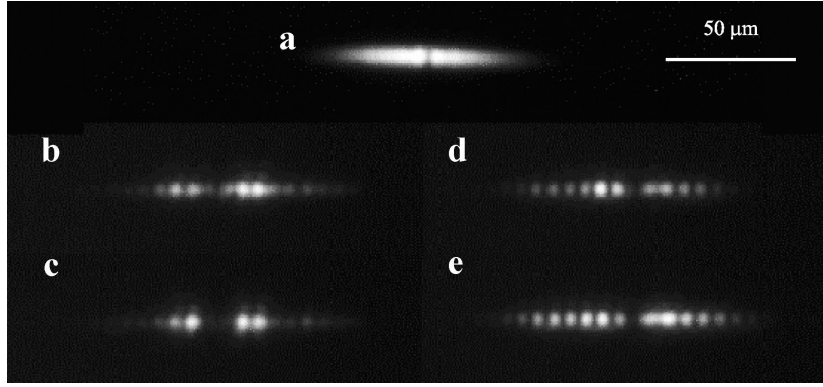


Figure 2.15: Generation of a dark discrete solitary wave in the case of anomalous diffraction. **(a)** The input profile, $\sim 40 \mu\text{m}$ wide at FWHM. **(b)** For normal diffraction at low power, a notch is visible in the output profile. **(c)** The beam evolves into two repulsive bright solitons when the intensity is increased ($I_{\text{peak}} \sim 250 \text{ W}$). **(d)** For anomalous diffraction (beam tilt $= 2.0 \pm 0.4^\circ$ in this array), the “dark” notch is initially present in the output profile (linear case). **(e)** When the power is increased ($I_{\text{peak}} \sim 250 \text{ W}$), the notch slightly narrows and becomes more marked. As a result of anomalous diffraction, the dark localization is self-sustained in a defocusing bright background, and does not disappear when the beam broadens nonlinearly

notch in a constant background is formed at sufficiently high power – a dark soliton.

Dark solitons can be formed in two cases: the first is when diffraction is normal and n_2 is negative and the second is when diffraction is anomalous and n_2 is positive. As we have the right conditions for the second options, we tried to launch discrete dark solitons in our samples of waveguide arrays [19,20]. A π phase mask was applied on the beam right before entering the sample. The shape of the input beam with the dark notch is presented in Fig. 2.15(a). As in Fig. 2.13, we show results of normal incidence ($k_x = 0$) in Figs. 2.15(b,c) and results of the anomalous diffraction condition ($k_x = \pi/d$) in Figs. 2.15(d,e). In the normal regime, the low power notch (Fig. 2.15(b)) is broader than one waveguide and somewhat blurred. At power that is sufficient to form a bright soliton (Fig. 2.15(c)), the notch defocuses and becomes broader and more pronounced, while the finite bright background is focusing, as is expected in this regime. On the other hand, in the anomalous case the dark notch is preserved with power (Fig. 2.15(e)) while the finite bright background undergoes self-defocusing. These results are not a discrete dark soliton in a strictly manner because the background is not a constant illumination. Even more, in some of the results (Figs. 2.15(b–d)) the bright and dark widths are on a comparable scale. Nevertheless, they show some significant hints for this solitary phenomenon.

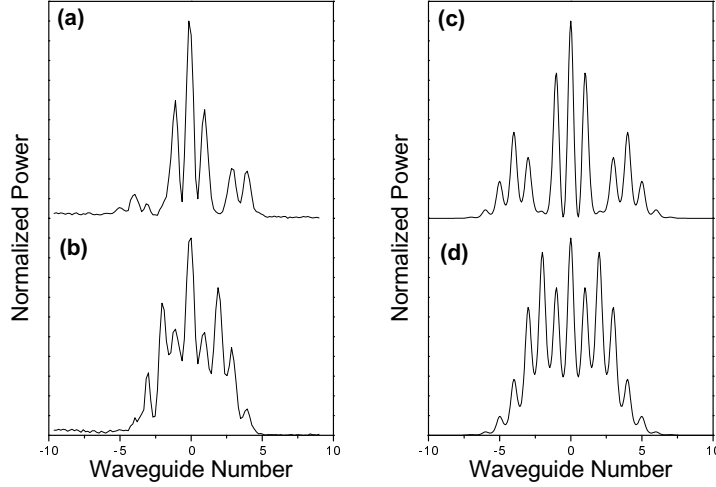


Figure 2.16: Experimental results of the defect sample for (a) low and (b) high power input. Numerical simulations for the same conditions are presented in (c) and (d), respectively

2.7 Nonlinear Interaction of a Linear Defect State with Discrete Diffraction

There is a well-known way to form a linearly localized state in a discrete system. In an infinite coupled array, when one waveguide has its propagation constant changed to $\beta + \Delta\beta$, a confined mode around this site is created [11, 12]. Usually, changing the propagation constant β would also affect the coupling constant to become $C + \Delta C$. The confined defect mode would have the shape:

$$E_n(z) = \frac{E^0}{\rho^{|n|}} \left(1 + \frac{\Delta C}{C} \right) \exp(i\beta_{\text{defect}} z), \quad (2.2)$$

where the defect mode propagation constant is $\beta_{\text{defect}} = \beta + (\rho + 1/\rho)C$ and the transversal decay rate ρ is defined as:

$$\rho = \frac{\Delta\beta}{2C} - \sqrt{\left(\frac{\Delta\beta}{2C}\right)^2 + 2\left(1 + \frac{\Delta C}{C}\right)^2} - 1. \quad (2.3)$$

When light is launched into such a linear mode, the high power result depends on the value of β_{defect} compared to the discrete band $\{\beta - 2C < k_z < \beta + 2C\}$. If the defect mode is above the band ($\beta_{\text{defect}} > \beta + 2C$), then the Kerr effect will just raise it higher, without any dramatic consequences. When β_{defect} is in the band, the usual self-focusing is expected, similarly to the discrete soliton case. More interesting case is when the linear defect mode is below the

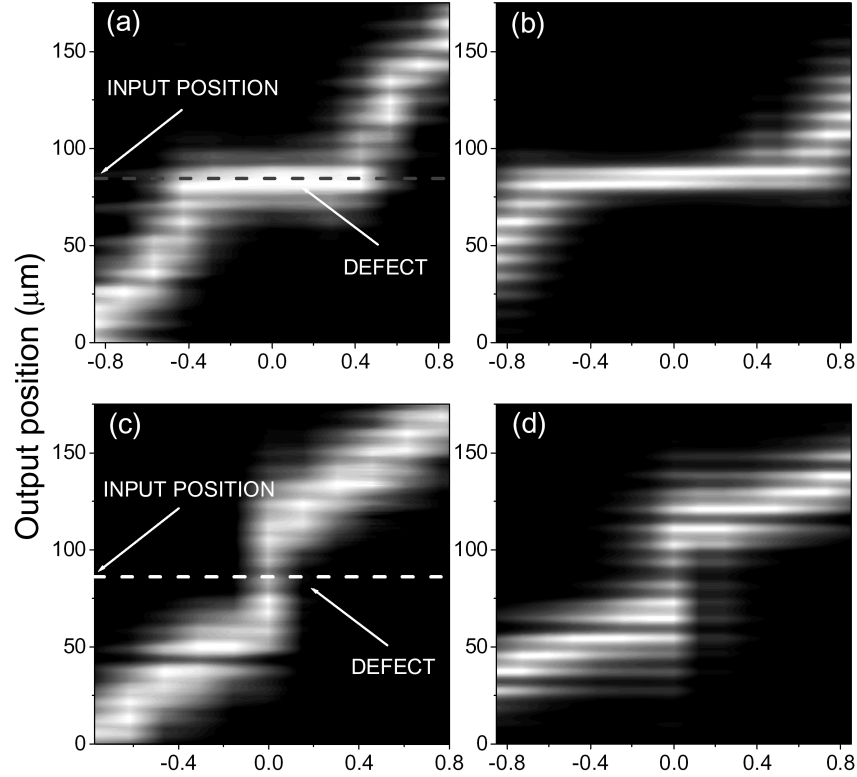


Figure 2.17: Interaction of a discrete soliton with defects. The soliton is injected exactly on the defect, which is represented by a *dashed line*; **(a-b)** attractive case, experimental results and simulations; **(c-d)** repulsive defect, experimental results and simulations

band ($\beta_{\text{defect}} < \beta - 2C$). In the linear regime there is confinement, as outlined before. As the injected power increases, the mode propagation constant enters the optical band, interacting linearly with it and enabling the dispersion of energy into more waveguides. It is the opposite effect of nonlinear self-focusing, but in this case, without the inversion of diffraction.

We tested a sample of waveguide array with a separation of $d=9\mu\text{m}$. Each waveguide was $4\mu\text{m}$ wide except for the central waveguide ($n = 0$) which was $2.5\mu\text{m}$ wide. This difference caused a local change of the parameters such that $\Delta\beta = -1.5C$ and $\Delta C = 0.3C$, resulting in a confined linear defect mode below the optical band ($\beta_{\text{defect}} = \beta - 2.9C$). The calculated decay rate is negative $\rho = -2.5$, forming π phase jumps between adjacent waveguides. The confined mode which was obtained by launching low power light only into the central waveguide is presented in Fig. 2.16(a). The π phase jumps give rise to the strong

visibility of the three central waveguide modes. The weak wings are formed because the input light did not overlap completely the defect mode, therefore leading to radiation evolving through usual discrete diffraction. As the power is increased (Fig. 2.16(b)), The defect mode starts to interact with the diffraction band, and light is escaping out. The light distribution is becoming wider from about three waveguides to about seven. The same results are demonstrated numerically in Figs. 2.16(c,d).

Next, we checked the effects of the two types of defects, i.e. attractive and repulsive, on the transport of angled discrete solitons [55]. An input beam, $12\mu\text{m}$ wide was injected at the soliton power on the site of a defect. The beam angle was scanned in order to observe the defect effect on the soliton. The results are presented in Fig. 2.17. Figures 2.17(a-b) are respectively experimental and numerical results for an attractive defect whose effective index is above the diffraction band. Respectively, figures 2.17(c-d) are for a repulsive defect whose effective index is below the band, like the one described in the previous experiment. The effect on the soliton steering is clear. The attractive defect enhances the power locking of the soliton to its origin by linearly deepening the PN potential. It is now even harder for a discrete soliton to start travelling across the array. On the other hand, a repulsive defect releases the soliton by linearly flattening the blocking PN potential. At zero angle input, the beam nonlinear broadening is evident. Compare this broadening to the enhancement in confinement at the same angle for the attractive defect case. The comparison to the numerical results in both cases is remarkably good.

Chapter 3

Linear Effects in Inhomogeneous Arrays

Even though nonlinear optical solitons were the motivation for this research, they drove us to other territories. We were appealed by the option to check situations where diffraction is not as in continuous everyday media. Engineering the free parameters of waveguide arrays opens new possibilities for even linear optics.

In this chapter, three schemes of altering the regular array structure are presented. The consequences of such diffraction control on nonlinear dynamics are discussed. We start with a linear index chirp and the resulting optical Bloch oscillations. The next section deals with randomization and its effect on localization. Finally, we suggest a recipe for creating a waveguide of any desired diffraction relation.

3.1 Bloch Oscillations

The effect of Bloch oscillations is known for many years [56]. It is manifested by electron oscillations in a crystal lattice under a linear cross-potential of an electrical field. The cause for the periodic behavior is an interplay between the accelerating field and the discreteness of the atomic lattice. Due to discreteness, electrons experience a periodic dispersion relation and a Brillouin zone is defined [42]. As the electrons are accelerated, they approach the border of the Brillouin zone. When they pass this border, they emerge from the other zone side, effectively returning to their origin.

A better understanding of this phenomenon can be achieved by examining the eigen-states of this system. It appears that the non-localized Floquet-Bloch states of the free discrete lattice, transform into localized states under the application of the linear potential – the Wannier-Stark states. Moreover, these localized states are energetically equally spaced, known as the Wannier-Stark ladder. Therefore, for any initial excitation of this system spanned by this

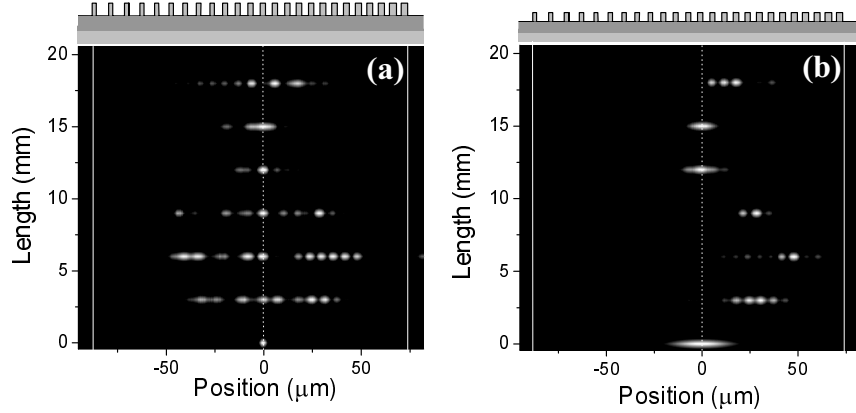


Figure 3.1: Results at low power input for the Bloch oscillations experiment. Subsequent outputs are from samples whose length differ by 3 mm. (a) A single waveguide input 3 μm wide and (b) a wide input of 20 μm . The output power distribution is shown as a function of the propagation length. The optical field is reforming to its input after 12 mm

set of functions, there must be a certain time of evolution when all the functions accumulate a phase which is an integer multiple of 2π . This is the time when the initial excitation will be recovered.

Recently, the equivalence between electrons in atomic lattices and optical waveguide arrays has been pointed out. Each single mode waveguide represents an S-level atom within the tight binding approximation. The coupling between neighboring atoms is replaced by the overlap of the waveguide evanescent modes. Furthermore, if an effective linear cross-potential can be applied, Bloch oscillations were predicted [33]. The implementation of a linear potential is by a linear change in the refractive index. The two balancing causes for the deflection of an optical excitation are Snell's refraction and Bragg's reflection. The equations of motion are identical to Eqs. 1.1, except for a waveguide dependent propagation constant:

$$\beta \rightarrow \beta_n = \beta_0 + n\delta\beta. \quad (3.1)$$

In order to apply the required linear cross-section of refractive index, a few methods have been proposed. One method is to apply a voltage gradient across an array that is made of an electro-optical material [33]. The linear electrical field induces a proportional index change through the electro-optic effect. The slope of the index change is voltage dependent. Another method, which was used in one experimental realization [36], is to apply a temperature gradient across a thermo-optically active material. Again, the temperature changes the refractive index, resulting in the desired index change.

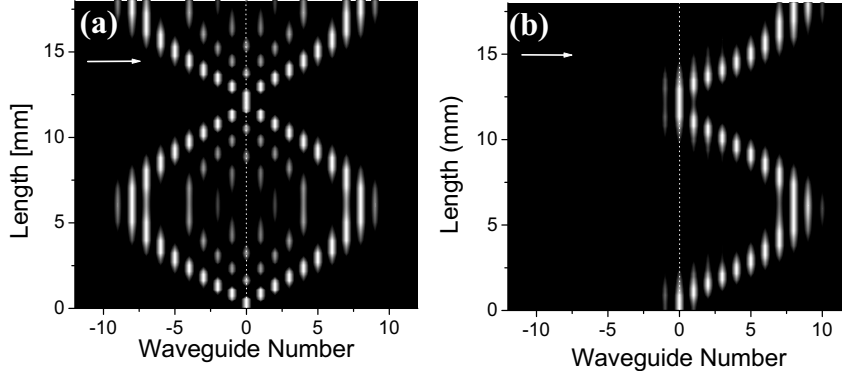


Figure 3.2: Numerical results at low power input. (a) A single waveguide input $3\mu\text{m}$ wide and (b) a wide input of $20\mu\text{m}$. Results compare well with the experiments (Fig. 3.1)

Two other methods to form a linear index gradient by structural patterning of the arrays were suggested. One idea is to induce an effective index slope by using a regular array of curved waveguides [34]. Under a transformation that straiten the waveguides, the curvature transforms into the desired effective potential. Another idea, the one that was used by us, is to construct the array such that each waveguide has a different width [35]. The width determines the waveguide effective index, and if designed well, a gradual increase in the waveguide widths may lead to a linear increase in their effective indices. As the individual mode shape is changing with the width too, attention has to be given to the separation between every two waveguides in order to keep constant coupling.

We fabricated arrays of 25 waveguides with width variation between 2 to $3.4\mu\text{m}$. The waveguide spacing was respectively changed between 6.6 to $3.3\mu\text{m}$. The coupling constant was $C = 1240\text{m}^{-1}$ and the propagation constant step was $\delta\beta = 520\text{m}^{-1}$. Samples of different lengths between 3 to 18mm were cut with a step of 3mm . The samples were tested in a similar way to previous experiments such as in the demonstration of discrete solitons. The two basic linear observations are presented in Fig. 3.1. In Fig. 3.1(a), a single waveguide input (an excitation of all the spatial frequencies in the Brillouin zone) is diffracting and reforming after propagation of 12mm . A wide input (a narrow frequency excitation, see Fig. 3.1(b)) is oscillating transversely with the same period. The wide beam is accelerated towards the higher index zone (wider waveguides). Near the edge of the Brillouin zone the phase difference between adjacent waveguides is close to π , as is proven by the high visibility of the individual waveguide modes. The experimental results can be compared to a numerical integration of the equations of motion (See Fig. 3.2).

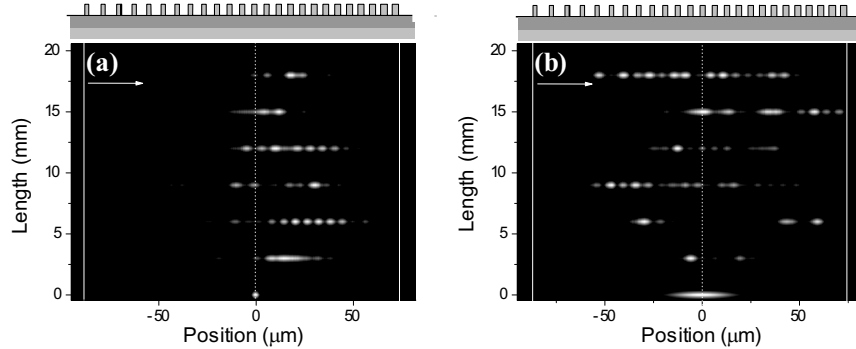


Figure 3.3: High power experimental field evolution (about 2000 W peak power). Results were taken with the same parameters as in Fig. 3.1

As the oscillations depend strongly on the exact phase relations between the different modes, any perturbation on the optical phase will destroy this behavior. Such a perturbation can happen due to random scatterers in the light path. The nonlinear Kerr effect can also change the phase of individual waveguides according to the amount of optical power they carry. There is an analogy between the two effects [57]. In the presence of this effect, no reformation of the light distribution can occur. Experimental results from the same sample, but for high power input, are presented in Fig. 3.3. Because of the Kerr effect the waveguides that contain power have higher index. This index change makes them resonate with the waveguide to their right (the wider waveguide) and generally we can observe a tendency of light coupling towards this direction. Bloch oscillations are destroyed. The next section provides another connection between random scattering and nonlinearity.

3.2 Anderson Localization

Looking further at the similarities between atomic crystals and optical waveguide arrays, we examined the effect of randomness on nonlinear localization [58]. It is well known that as random elastic scatterers are added to a crystal, the non-localized electron wave-functions (the Bloch states) are becoming localized [59]. As a result, an initial excitation would find it more difficult to transport along the crystal. Above a certain threshold of the amount of randomness, transport becomes impossible and the crystal behaves like an insulator [60]. This effect is called Anderson localization.

Scattering centers could be introduced in crystals by growth defects. The equivalent of a crystal defect in the waveguide array case was already described in section 2.6. A waveguide defect changes only the phase of the light that is passing through it, thus behaving like an elastic scatterer. Filling the whole

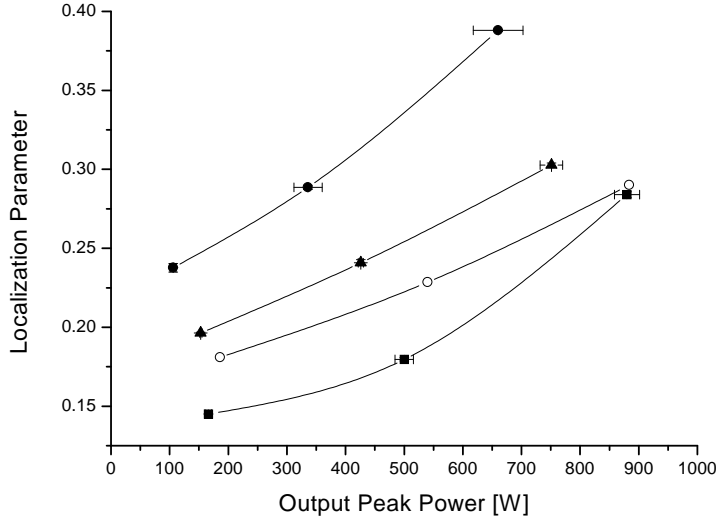


Figure 3.4: The dependency of localization in random arrays as a function of randomness and nonlinearity. In all arrays, localization is becoming larger as the input power is increased. Output from longer effective length arrays is less localized (coupling lengths of 3.82, 5.15 and 7.30 are presented by *solid circles*, *solid triangles* and *solid rectangles*, respectively). Random arrays are clearly confining light better than the regular array (3.84 coupling lengths, *open circles*). Note how the localization in the regular array is less affected by nonlinearity

array with such defects would be realized by randomly changing the width of all the waveguides. The optical super modes of the array are becoming more localized as more randomness is introduced. Now, any localized input light is spanned by a limited number of modes, thus preventing the light from evolving into more distant waveguides, as would happen in a regular periodic array.

As was shown before, the nonlinear Kerr effect also results in localization. We were interested in examining the interplay between these two phenomena. Four types of arrays were fabricated: three arrays of random widths and one with a constant width. The regular array had $4\ \mu\text{m}$ wide waveguides, spaced by $4.5\ \mu\text{m}$. Comparing light propagation in this array with a coupled-mode theory simulation [1], the effective propagation length of this sample was calculated to be 3.84 coupling lengths. Then, using beam propagation method (BPM)¹ [61], the effective indices of the sample were fit. All the random arrays waveguide widths were distributed evenly over the range of $2.5\text{--}4.5\ \mu\text{m}$. The waveguide spacing were 2,3 and $4\ \mu\text{m}$. Effective length were calculated for the three random samples by assuming the average width of $3.5\ \mu\text{m}$, the different spacing and the calculated effective indices. The lengths are 7.30, 5.15 and 3.82 coupling lengths

¹*FreeBPM*, a freeware windows application that was developed during this Ph.D. work, is available at <http://www.freebpm.com>

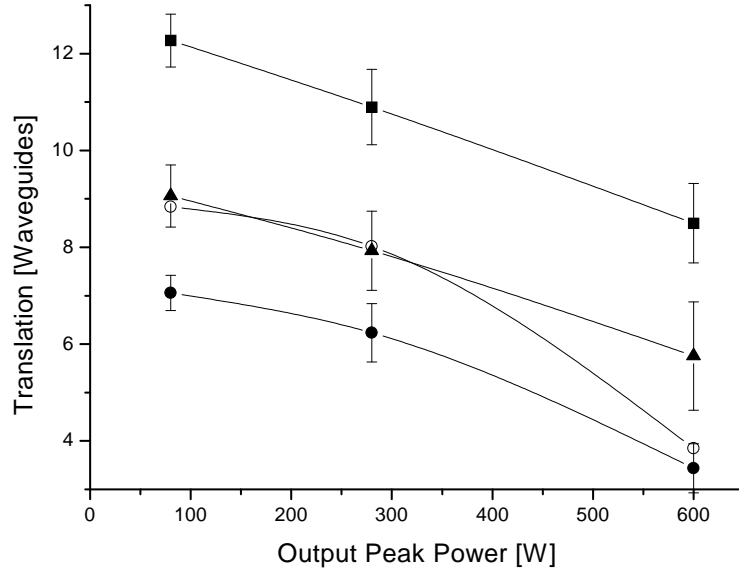


Figure 3.5: The dependency of lateral translation of a tilted beam in random arrays as a function of randomness and nonlinearity. In all arrays, translation is becoming smaller as the input power is increased (power steering). Output from longer effective length arrays is more translated (symbols represent the same parameters as in figure 3.4). Random arrays are better ‘insulators’ than the regular array

for the 2,3 and 4 μm samples, respectively. All arrays had 61 waveguides.

Like in the previous experiment of Bloch oscillations, we checked the evolution of two types of input. The first is a narrow, single waveguide input, which excites all spatial frequencies. Such an input should experience the largest amount of diffraction and spread over the largest possible extent. As random arrays would give a random behavior, and therefore random output light distributions, ten output profiles of input at different positions across the array, were averaged for every measurement. The full width at half the maximum or a gaussian fit methods for estimating the width of a function are not suitable in this case because of the irregular light distributions (not bell-shaped) of even regular arrays. Thus, we calculated the amount of broadening for each distribution by defining a localization parameter \mathcal{L} :

$$\mathcal{L} = \frac{\sum_n I_n^2}{\left(\sum_n I_n\right)^2}. \quad (3.2)$$

\mathcal{L} is becoming larger as light occupies smaller number of waveguides. It is unity at the input, and decreasing thereafter. Any localization process should result with increase of the localization parameter.

The measurements of the localization parameter at various input powers and in the four different arrays are summarized in figure 3.4. We observe all types of expected behavior. In general, light is becoming more localized as optical power is increased, while the opposite happens as it propagates further. Randomness is a localizing factor for all intensities, as the light from the random array of 3.82 coupling lengths (solid circles) is much more confined than that from the regular 3.84 coupling lengths array (open circles). More intriguing is the fact that the sum of the two localization mechanisms is greater than its constituents. All the random arrays show a faster localization with increasing power than the regular array.

A second type of input condition was checked in order to explore the transport properties of light across the random arrays. A tilted wide beam of a few waveguides width was allowed to propagate while hopping across the array. Its angle was tuned to the $k_x d = \pi/2$ condition (see figure 3.5) where the largest lateral shift should occur. The amount of lateral translation was measured by the center of mass of the output distribution:

$$X = \frac{\sum_n n I_n}{\sum_n I_n}. \quad (3.3)$$

These results are reproducing all the expected features. As the input intensity is raised, power steering (see section 2.5) limits the amount of beam translation. Randomness proves to be an insulation factor because the beam translated more in the regular array than in its random counterpart. The results at high intensity should be regarded with care, as at these conditions the beams tend to scatter considerably in the random arrays. A consequence of this is that high power locks the beam more efficiently in the regular array.

This experiment had an underlying fault: a small number of couples of adjacent waveguides were too close to each other. As a result, a couple like that has one mode instead of two, therefore behaving like a single waveguide. The results still hold in general, as the occurrence of this problem was quite rare.

3.3 Diffraction Management

The existence of a periodic diffraction relation in waveguide arrays suggests new possibilities in linear and nonlinear beam manipulation. After showing many nonlinear phenomena in this discrete optical system, we have investigated some linear properties. In particular, the most novel linear property is the diffraction sign inversion in the $\pi/2 < |k_x d| < \pi$ regime [62]. Recently, a similar effect was shown to happen also in photonic crystals [63].

The diffraction of linear light beams is analogous to the effect of dispersion on the temporal evolution of optical signals. In fact, we already used terms which were taken from dispersion theory, e.g., the anomalous diffraction. One important task in fiber optics research is dispersion control. The fiber index profile can be engineered in order to achieve certain amount of dispersion, or

even to reverse its sign [64]. In the last years, fast development of new ideas in dispersion control [65–67] was motivated by its importance to optical communication. We borrowed a central scheme used in dispersion control in order to design planar waveguides of engineered spatial diffraction.

Because dispersion and diffraction are linear operations, the two different operators are commutative, thus affecting the system through their sum. The outcome of propagating through two different regimes of dispersion do not depend on which was first. If both lengths are equal, the overall experienced dispersion is the average of the two. Dispersion management uses a set of different length fibers with different dispersion properties [65]. The lengths are designed such that by travelling through all fibers, optical pulses experience a pre-defined overall dispersion.

It is the existence of anomalous diffraction in waveguide arrays that enables a similar design of diffraction. Diffraction management is even more mathematically straightforward, as discrete diffraction curves, under coupled-mode theory, are always cosine functions. By fabricating a planar waveguide composed of sections of different patterns of arrays, it is possible to engineer diffraction. Light would travel through such structures the same way as travelling through a waveguide of averaged homogenous diffraction of the form:

$$\langle k_z \rangle (k_x) \cdot L = \sum_i k_z^{(i)}(k_x) \cdot l_i = kL + \sum_i 2l_i C_i \cos(k_x d_i + \theta_i) , \quad (3.4)$$

$$L = \sum_i l_i \quad \theta_i = k d_i \sin(\alpha_i) , \quad (3.5)$$

where l_i is the length of the i^{th} section and $k_z^{(i)}(k_x)$ is its diffraction relation. The array section's coupling constant, waveguide separation and angle to the \hat{z} -axis are C_i , d_i and α_i , respectively. By using 0 and $\pi/2$ values for θ , any arbitrary periodic function can be spanned by its sine and cosine Fourier elements. For example, a periodic triangular diffraction relation is spanned by the series $\sum_n \frac{\cos[(2n-1)k_x d]}{(2n-1)^2}$. In such an ideal array, light power is allowed to propagate in only two directions while experiencing no diffraction. A reasonable approximation for such a function can be obtained by alternating only two kinds of arrays with separation ratio of $d_1/d_2 = 3$ and length ratio of $l_1/l_2 = 9C_2/C_1$.

In order to demonstrate diffraction management, we fabricated waveguides of engineered reduced diffraction, no diffraction and anomalous diffraction. The waveguides were made of only two kinds of equal length, alternating sections. All of the two section parameters were identical except for α , their angle with the \hat{z} -axis. This angle had constant absolute value, but alternating sign. As α is becoming larger, diffraction is reduced, until it is zero when $\alpha = \arcsin\left(\frac{\pi}{kd}\right)$. Beyond this point, diffraction becomes anomalous.

We fabricated such zigzag arrays of angles corresponding to $\theta = 0, \pi/4, \pi/2, 3\pi/4$ and π . The advantage of such zigzag configuration over just a tilted array is the symmetric cancellation of the diffraction high orders. For example, although a tilted array of $\theta = \pi/2$ has a zero diffraction at zero incident angle, higher derivatives of the diffraction curve still exist and can contribute to an

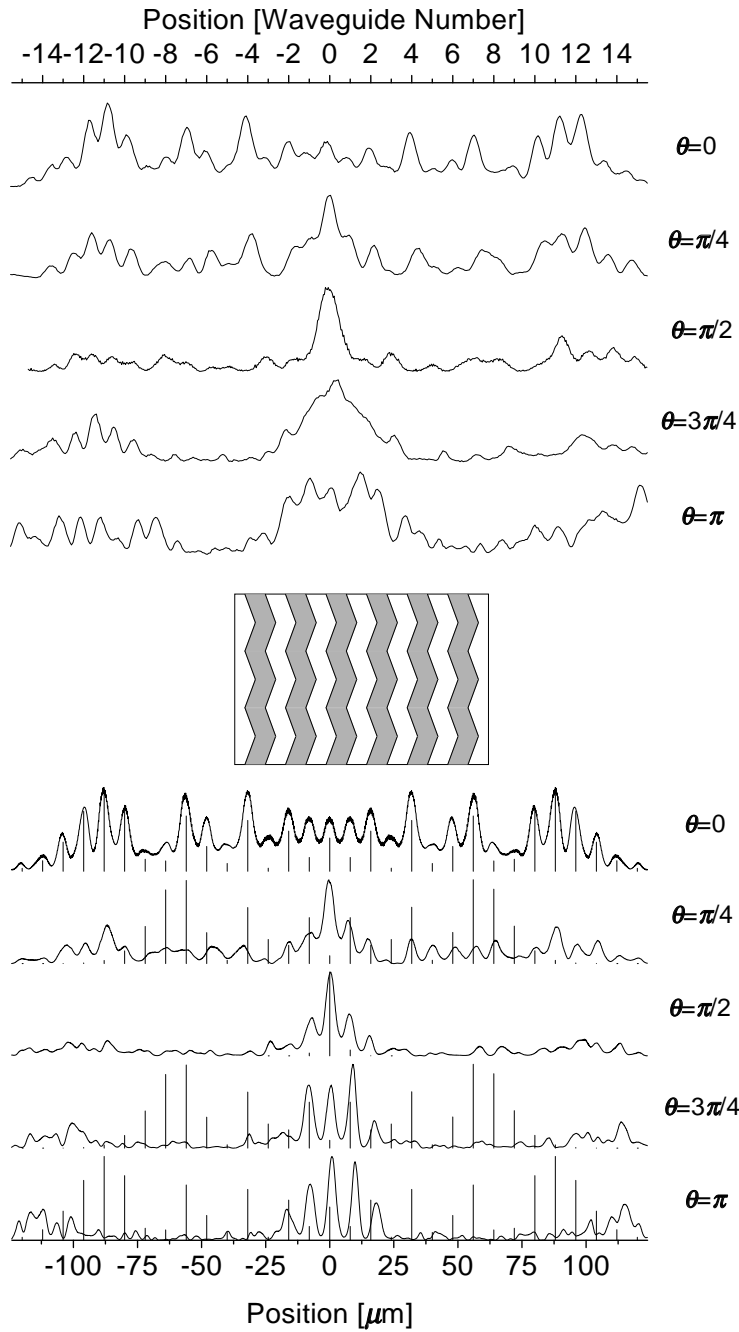


Figure 3.6: Output intensity profiles after propagation of a $5\ \mu\text{m}$ wide input through zigzag arrays. **Upper graph:** Experimental results for various tilt angles. **Lower graph:** calculated output by beam propagation method (*continuous lines*) and coupled-mode theory (*vertical bars*). **Inset:** a sketch of the waveguides

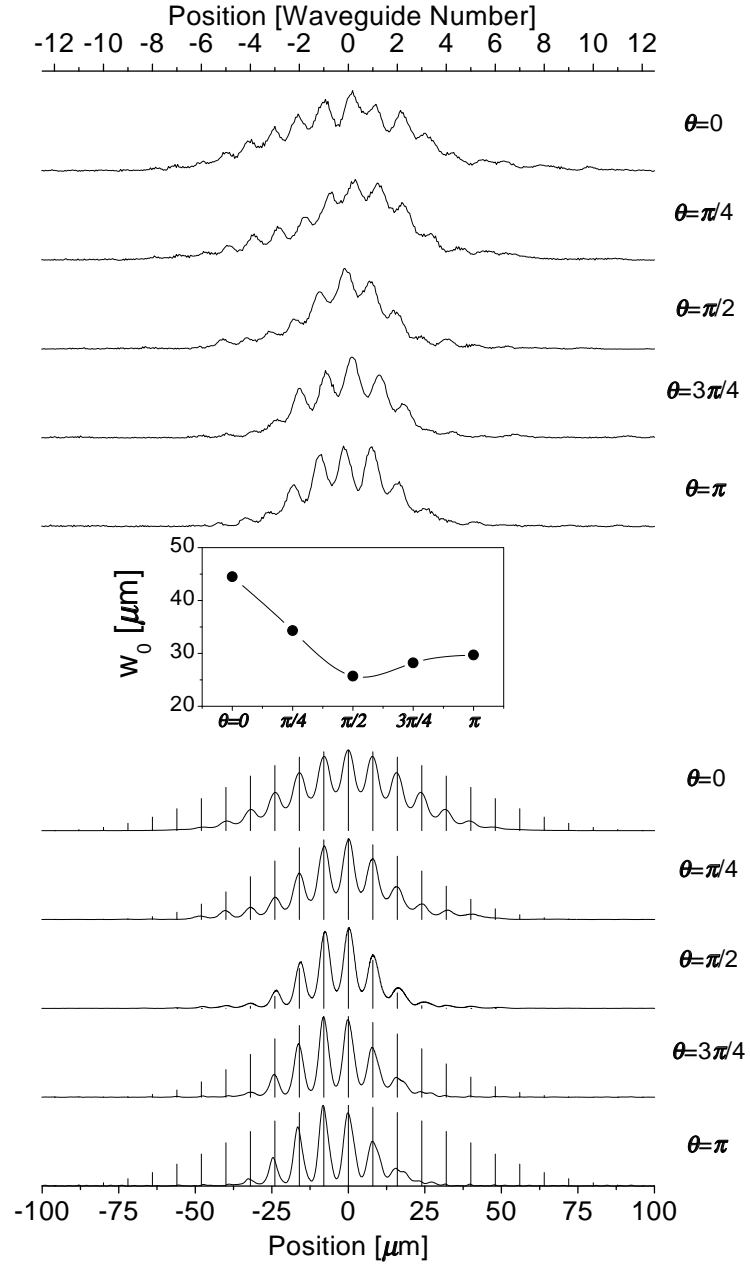


Figure 3.7: Same as Fig. 3.6 for a $21\mu\text{m}$ wide input. **Inset:** widths for the experimental output profiles

asymmetric broadening of an initial beam [68]. In the zigzag array of the same angle, light in *any* angle experiences no diffraction whatsoever.

The results of propagation of narrow, single waveguide input in these arrays are described in the upper part of Fig. 3.6. Zero zigzag angle is simply a plain straight array. At the zero diffraction case ($\theta = \pi/2$), light is barely coupled into other than the input waveguide. Beyond this angle, the broadening is a result of anomalous diffraction. Some light is scattered at the sharp turns and the desired effect is reduced. This flaw may be corrected by arrays of smoother corners. The lower part of 3.6 compares numerical results of propagation in the arrays. We used simulations of two kinds: a coupled-mode based numerical solution [1] and a beam propagation method [61] solution. The BPM is more realistic as it considers more details, and therefore more consistent with the experiments.

The output distributions from a wider input that covers several waveguides are presented in Fig. 3.7 in a similar way. Although a broader beam is affected less by diffraction, some broadening is measured. The inset of Fig. 3.7 proves that the array of designed zero diffraction induces the minimal beam broadening.

Some of the potential applications of nonlinear beams in such designed waveguides are already demonstrated by the results presented in section 2.6. The idea of dispersion managed solitons [66, 67] can be applied in the space domain to produce diffraction managed solitons. Reference [69], that was published as a consequence of this work, discusses this situation.

Chapter 4

Kerr Spatiotemporal Self-Focusing

The propagation of intense ultrashort light pulses has received a lot of attention over the last decade. It is influenced by the interplay of various physical mechanisms, the most important being diffraction, material dispersion, the nonlinear Kerr effect and nonlinear absorption [70]. One of the most intriguing cases is when diffraction and dispersion have the same sign and magnitude. Measures to these magnitudes are the typical propagation lengths it takes a pulse to expand. The diffraction and dispersion lengths are defined respectively as:

$$L_{\text{Dif}} = k_0 L_0^2 \quad L_{\text{Dis}} = \frac{T_0^2}{\beta_2} . \quad (4.1)$$

$\beta_2 = \frac{\partial^2 k}{\partial \omega^2}$ is the material chromatic dispersion while L_0 and T_0 are the pulse initial width and length, respectively. In the linear regime, equal diffraction and dispersion lengths results in a pulse that expands uniformly in space and time. At high light intensity in a nonlinear medium, the Kerr nonlinearity simultaneously compensates for both effects by self-focusing in space and self-phase modulation (SPM) in the time domain. Consequently, pulses undergo spatiotemporal contraction and may form optical light bullets [71]. Such a case occurs in materials with positive Kerr coefficient and anomalous dispersion.

Basic analysis of the propagation of multi-dimensional pulses, involving the slowly varying envelope approximation, predicts instability [71]. Such pulses are categorized as ‘1+2’ and ‘1+3’ cases, depending on whether diffraction is limited to one dimension, as in a planar waveguide, or to two as in a bulk medium. A pulse having power beyond a critical value is predicted to contract to a singular solution. However, such mathematical collapse is usually avoided in experiments because of other effects which become significant, e.g., higher order nonlinearities such as multi-photon absorption [72] and saturation of the Kerr nonlinearity [73]. Light bullets are solitary light pulses that propagate

while retaining their shape in all dimensions. They are a combination of the well known spatial and temporal solitons.

4.1 Experimental Results

Recently, a few experiments attempted to demonstrate simultaneous spatiotemporal focusing. Nevertheless, all the nonlinearities used were other than Kerr. Liu *et al.* [74] used the cascading of quadratic nonlinearity to create a bound pair of fundamental and second harmonic pulses, co-propagating while balancing each other's spatiotemporal shape. In another experiment [75], the balancing of normal dispersion by its higher orders and the Kerr nonlinearity, was shown to form stable three dimensional pulses in a bulk media. Pulse splitting in the normal dispersion regime, where self-phase modulation broadens the pulse temporally, was also demonstrated experimentally [76].

We studied experimentally the propagation of intense ultrashort pulses in the '1+2' case, i.e., in a planar glass waveguide, where the Kerr nonlinearity is predominant [77]. The nonlinear behavior in the different regimes of anomalous, zero and normal dispersion was compared [78]. Only in the anomalous case the pulses focus simultaneously in space and time. Nevertheless, we did not observe the predicted catastrophic collapse [71]. In fact, beyond a certain power at which the spatial and temporal profiles are the narrowest, the pulses start to expand. We present numerical studies showing that the main causes for this behavior are multi-photon absorption [72] and intra-pulse Raman scattering [79,80]. Based on this model, we believe that after the pulse reaches its minimal size, it propagates in a way that resembles the propagation of light bullets. However, our results also suggest that such pulses can not propagate indefinitely, since the same effects that arrest their collapse eventually cause their expansion. This is the first time that spatiotemporal focusing has been experimentally observed in a Kerr medium.

In the experiment we coupled transform limited 60 fs pulses, with peak powers up to 20 MW, from a Spectra Physics OPA 800 optical parametric amplifier, into planar glass waveguides. We used a combination of microscope objective and cylindrical lenses to achieve an elliptical beam, about 170 μm wide, with a flat phase-front at the input facet of the sample. This combination also enables matching of the beam size, and thereby the diffraction length, to the dispersion length of such pulses in glass. The single-mode waveguide was 3 cm long, consisting of a 4 μm thick germanium-boron doped silica slab waveguide deposited by flame hydrolysis deposition on an oxidized silicon wafer with a 14 μm thick layer of SiO_2 . The output facet of the sample was imaged onto an infrared camera. A portion of the output beam was directed to a spectrometer. Another portion of the beam was directed to a non-colinear autocorrelator. The 100 μm thick BBO nonlinear crystal used in our autocorrelator enables accurate measurement of pulse durations down to 10 fs. The glass in the optical path to the autocorrelator introduced a systematic error to the pulse width measurements, which we estimate to be smaller than 10 fs. An aperture, placed in an image

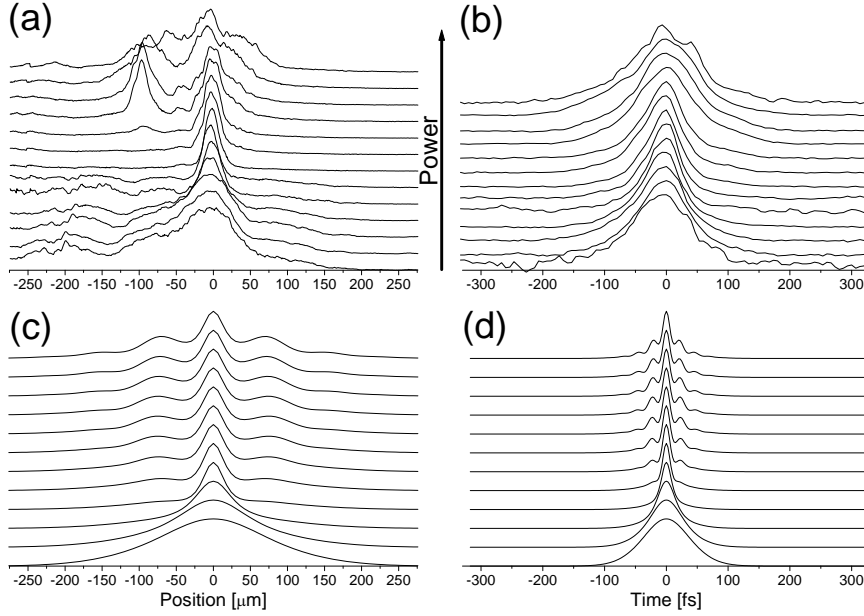


Figure 4.1: Normalized (a) Spatial profiles and (b) temporal autocorrelation traces of the light pulses in the anomalous dispersion regime, emerging from the sample. The profiles are arranged so that results at higher input powers are plotted sequentially upwards. Spatial and temporal contraction are obtained simultaneously for peak powers of 600 kW. For a comparison with the numerical results, see (c) for spatial profiles and (d) for on-axis temporal autocorrelation traces

plane of the output facet, allowed temporal and spectral characterization of the central part of the output beam. We repeated the experiment at three different wavelengths, 1.52 μm (anomalous dispersion), 1.30 μm (zero dispersion) and 1.04 μm (normal dispersion).

The results for the anomalous dispersion case, with the laser tuned to 1.52 μm , are shown in Fig. 4.1. Figure 4.1(a) shows the beam spatial profile at the output facet for different values of power. As the power of the incoming beam is increased, the beam width first contracts to about 20 μm , then remains nearly unchanged as the power is increased. Eventually, the beam slightly broadens while breaking up into filaments which broaden and merge. The corresponding autocorrelation traces (Fig. 4.1(b)) also show a contraction by a factor of nearly two. The narrow pulse which is formed (20 $\mu\text{m} \times 30$ fs) seems to be stable for a range of input intensities. It is important to note that the temporal profile and the spatial cross-section evolve simultaneously, reaching their minimum values at the same power. This can be clearly seen in Fig. 4.3, where the beam parameters are plotted as a function of the peak power.

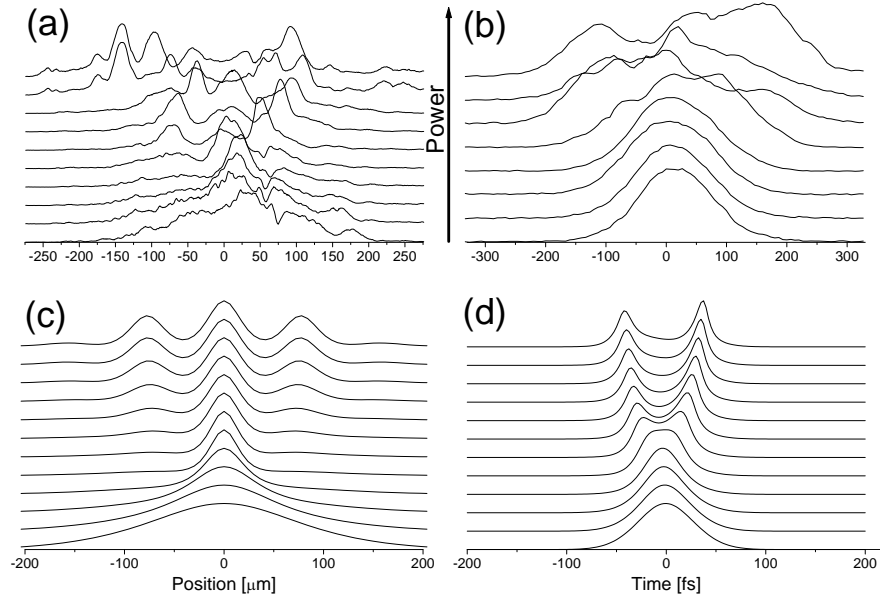


Figure 4.2: Experimental results for the zero dispersion regime, displayed as in Fig. 4.1

Both parameters exhibit a shallow minimum around 600 kW. This value should be compared with a value of 160 kW for which collapse is theoretically predicted for the parameters of our experiment [71].

The pulse does not collapse and no damage was observed, as would be expected for a pure Kerr nonlinearity and anomalous dispersion model. As we discuss below, numerical simulations suggest that this is due to the significance of multi-photon absorption and Stimulated Raman Scattering (SRS). These processes account for the higher than expected power required to induce spatiotemporal contraction, as well as for the eventual expansion of the pulses. We attribute the filamentation of the beam at high powers to instability due to imperfections in the input beam profile. Simulations suggest that even with a smoother profile, filamentation occurs at high power because of instabilities induced by nonlinear absorption [81].

When the laser was tuned to the zero dispersion regime of glass, a completely different pulse evolution was observed (see Fig. 4.2). The spatial focusing, although still present, is remarkably unstable. Beyond a short stage of beam focusing, its profile breaks into multiple fragments, even before reaching minimal width as in the anomalous case. There is no stability power range whatsoever. The temporal pulse evolution differ even more from the anomalous case. No temporal contraction occurs at all. In this case, the result of nonlinearity is pulse broadening. Because initially all frequencies are laid around the zero

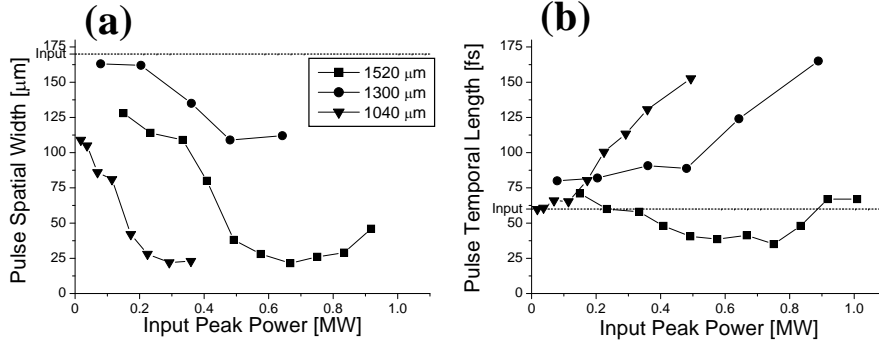


Figure 4.3: A comparison of the output pulses (a) spatial and (b) temporal widths in the three different dispersion regimes. The pulses contract temporally only in the anomalous dispersion regime (*rectangles*), while in the zero (*circles*) and normal (*triangles*) dispersion regimes there is nonlinear temporal broadening. In the zero dispersion case, temporal broadening occurs only after self-phase modulation creates enough spectrum at wavelengths far away from the zero dispersion wavelength

dispersion zone, pulse broadening is possible only after a short stage when temporal frequencies are created nonlinearly in the pulse. At the same time when the beam experiences filamentation, it also splits temporally. This is shown as the multi-peak autocorrelation, because three peaks in an autocorrelation correspond to two peaks in the time domain. A qualitative verification of these results is given by the numerical simulations, as compared in Figs. 4.2(c,d). The experimental results when the laser wavelength was tuned to the normal dispersion regime of glass, resembled qualitatively the behavior seen near the zero dispersion point.

A summarized comparison of the pulse evolution in the three different dispersion regimes is presented in Fig. 4.3. The measured spatial and temporal widths for the three different wavelengths are presented in Figs. 4.3(a) and 4.3(b), respectively. Spatial width data is presented only for input powers below which filamentation does not occur. Evidently, spatial self-focusing is observed in all three cases, but temporal contraction only occurs in the case of anomalous dispersion. Rather than becoming shorter, a significant increase of the pulse duration is observed for normal dispersion [53]. For zero dispersion, no pulse broadening occurs initially, as was shown before. Yet, as the pulse spectrum expands through self-phase modulation at higher powers (see Fig. 4.5 below), most of the energy in the pulse is pushed out of the zero dispersion regime, and the pulse begins to broaden. As a result, the spatial contraction is effectively one-dimensional in the normal and zero dispersion regimes, while it is two-dimensional in the anomalous dispersion regime. The higher power which is needed to achieve spatial contraction in the anomalous dispersion regime is

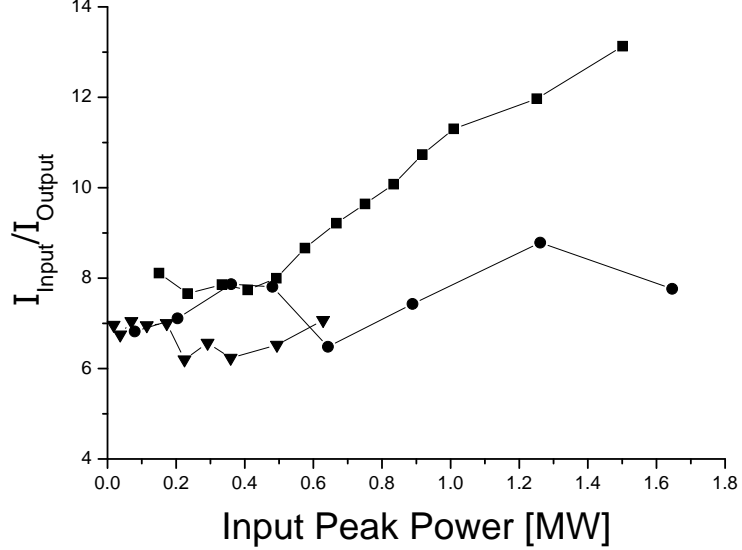


Figure 4.4: Losses in the sample. Only in the case of anomalous dispersion are intensities high enough for nonlinear absorption achieved. The background linear loss (about 7) is due to the in and out coupling to the waveguide

consistent with its higher dimensionality [71]. Simultaneous spatial-temporal contraction results in higher intensities, leading to stronger multi-photon absorption and also contributes to the increased power requirement. Indeed, as shown in Fig. 4.4, only in the anomalous case we observed significant nonlinear loss.

There is an asymmetry between the compression achieved in space and in time, as seen in Fig. 4.3(a,b). We attribute it to the wavelength limit on spatial and temporal focusing. The spot-size limit for focusing is about one wavelength. The minimal beam width that was observed in our experiment is about 20 times wider than the wavelength in the medium. On the other hand, in the time domain the minimal pulse length of 30 fs contains only about 6 optical cycles. Thus, higher orders of dispersion become important and affect the rate of compression.

Figure 4.5 shows the measured spectra as a function of increasing power. The spectra for anomalous, zero and normal dispersion are plotted in Figs. 4.5(a), 4.5(b) and 4.5(c), respectively. In all three cases the spectra at low power closely resemble those of the respective input pulses, while at high power they broaden considerably through self-phase modulation. In the anomalous dispersion regime the broadening is accompanied by a pronounced Raman self-frequency shift towards longer wavelengths [82,83]. Stimulated Raman Scatter-

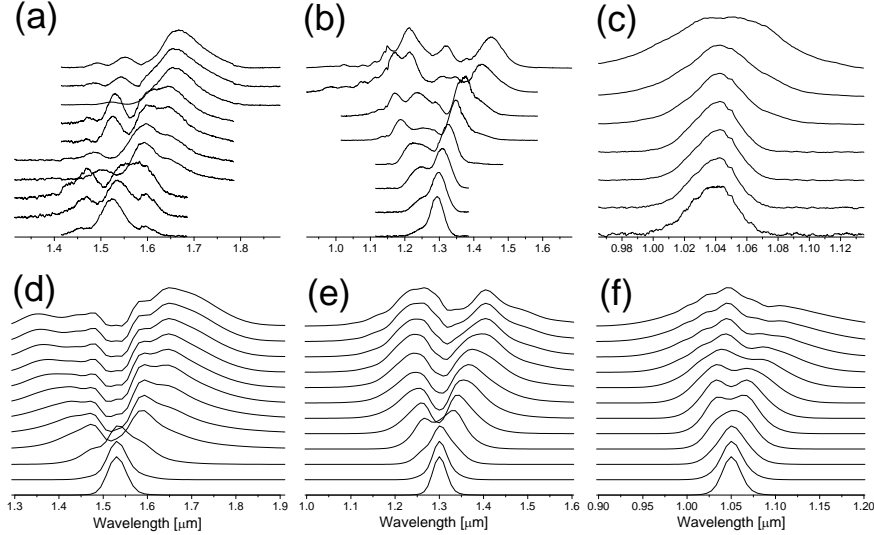


Figure 4.5: Spectra recorded for (a) anomalous, (b) zero and (c) normal dispersion for increasing input power. Numerical results are compared in (d–f), respectively

ing (SRS) happens when a photon is scattered on an optical phonon, losing some energy and thus its wavelength is red-shifted. In contrast, near zero dispersion (Fig. 4.5(b)) a Stokes Raman scattering wing appears together with an anti-Stokes component [84]. The generation of anti-Stokes frequencies is unique to this regime because all three frequencies (input signal, Stokes and anti-Stokes) propagate with nearly the same group velocity. In the case of normal dispersion (Fig. 4.5(c)) the spectra are only characterized by a symmetric broadening, the signature of SPM alone. SRS is absent due to mismatch between the delayed nonlinear polarization which is mainly behind the pulse and the long wavelength Raman frequencies that travel faster towards its front. The difference in this mismatch between anomalous and normal dispersion pulse propagation is plotted in Fig. 4.6. The data presented in Fig. 4.5(a) was taken with a longer 5 cm sample, but this has only a small effect on the emerging spectra.

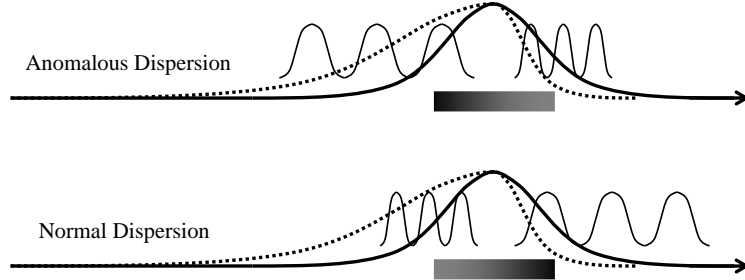


Figure 4.6: The reason Raman effects are dominant in the anomalous regime. The pulse (*solid line*) induces a delayed nonlinear polarization response (*dashed line*) which overlaps longer wavelengths of the pulse only in the anomalous case

4.2 Numerical Model

We compare these experimental results to numerical simulations. The numerical model is based on a modified nonlinear Schrödinger equation for the field amplitude E [53]:

$$i \frac{\partial E}{\partial z} = -\frac{1}{2k} \frac{\partial^2 E}{\partial x^2} + \frac{1}{2} \beta_2 \frac{\partial^2 E}{\partial t^2} + k \frac{n_2}{n_0} E \int_0^\infty R(t') |E(t-t')|^2 dt' - i \frac{\alpha_n}{2} |E|^{2(n-1)} E. \quad (4.2)$$

In this equation, k is the vacuum wavenumber, β_2 the dispersion parameter, n_2 the Kerr coefficient and α_n an n -photon absorption parameter. $R(t) = f_{\text{inst}} \delta(t) + f_{\text{delay}} h_R(t)$ includes the instantaneous and delayed parts of the Kerr nonlinearity. The delayed nonlinear response is known to approximate the Raman effect in silica [79] and may be written in the form $h_R(t) = \exp(-t/\tau_2) \sin(t/\tau_1)$ where $\tau_1 = 12.2$ fs and $\tau_2 = 32$ fs are the nonlinear polarization oscillations and decay typical time scales, respectively. The last term in the equation describes multi-photon absorption [72]. We chose $n = 6$ because six-photon absorption is expected to be the dominant term in glass for 1520 nm light.

A typical solution procedure is carried as follows. A typical complex grid of 256x512 in the space and time directions is initialized three times. One matrix is to contain the current scalar electrical field data, while the two others contain the current and previous material polarization. An initial pulse is written into the electrical field matrix and the program starts to propagate it. In every step, the following calculations are performed. First, the 2-dimensional data matrix is Fourier transformed to frequency space. The dispersion and diffraction effects are added as linear operations in this space. Then, the data matrix is transformed back to the real coordinate space. Here, nonlinear absorption is calculated. Consequently, the new nonlinear polarization is calculated at every

point using the previous step polarization and the current step electrical field by:

$$P_{\text{new}}^{\text{NL}} = P_{\text{old}}^{\text{NL}} \exp \left[\left(\frac{i}{\tau_1} - \frac{1}{\tau_2} \right) \cdot dt \right] + \tau_1 \cdot \left(\frac{1}{\tau_1^2} + \frac{1}{\tau_2^2} \right) |E|^2 dt . \quad (4.3)$$

Now, the effects of the instantaneous and delayed Kerr nonlinearity are introduced as a nonlinear phase shift to the electrical field:

$$E_{\text{new}} = E_{\text{old}} \exp [ik_0 n_2 (0.2 \cdot \text{Im}\{P_{\text{new}}^{\text{NL}}\} + 0.7 \cdot |E|^2) dt] . \quad (4.4)$$

The respective weights of instantaneous and delayed responses are taken from Ref. [79]. At the end of each step, some data is stored on the disk and the process starts over again. A typical simulation required 120000 steps. For main snippets from the original code, see Appendix B.

The model reproduced our experimental results quite well. First, we obtained spatial self-focusing in all the three regimes, as expected. In the time domain there is contraction only for the anomalous dispersion case, where for a large range of input intensities, after a transient length of about 1 cm, the pulse propagates with an almost stable spatiotemporal profile resembling a light-bullet. The zero and normal dispersion cases result in temporal broadening and eventually in pulse splitting, as predicted numerically [85] and recently observed experimentally [76]. Many features of the experiments were reproduced by the simulations. In particular, we obtained all the spectral features: self-frequency shift and spectral broadening in the anomalous case, Stokes and anti-Stokes scattering in the zero dispersion case and only spectral broadening due to self-phase modulation in the normal case. The spatial and temporal evolution for the anomalous and zero dispersion cases are presented in Figs. 4.1(c-d) and 4.3(c-d), respectively. The spectral evolution for all three cases is presented in Fig. 4.5. The good agreement between numerical simulations and our observations suggests that we have a good understanding of the dominant processes in these experiments.

Appendix A

Diffraction Curves

The concept of diffraction curves was introduced in section 1.3 in order to present and explain discrete diffraction. It provides a much more general tool for understanding linear optics and also some nonlinear effects. Its graphical nature can illustrate some basic principles while describing others in a precise geometrical manner. One known example where this approach is regularly used is in describing phase matching in non-centrosymmetric crystals by index surfaces [1]. Everything that will be shown here is applicable either in free propagation or under discrete optics conditions. Other situations, such as managed diffraction, are relevant as well.

For the sake of simplicity, we discuss in this appendix the free propagation case. As explained before, the diffraction curve that relates longitudinal to transverse spatial frequencies is a semi-circle. Actually, a whole circle describes the situation better by including backward propagating plane waves. Each point on the curve corresponds to a particular plane wave, whose Poynting vector (the direction of energy flow) is aligned perpendicular to the curve at that point.

The diffraction of narrow optical beams is now illustrated in a straightforward way. The profile of a confined beam contains a band of spatial frequencies, the narrower the beam the wider is this band. Assuming a symmetric profile, the packet is propagating along the Poynting vector of its central frequency (see Fig. A.1(a)). Nevertheless, other components of the beam are directed elsewhere, causing the beam to diverge. It is clear that as more components are included, as in a narrower beam, they are directed in a larger range of angles, resulting in a faster divergence of the beam energy.

The passage of light through an interface between two different materials is a basic problem in linear optics. We divide the problem into two parts, following the approach of Ref. [39]. The kinematic properties of the problem are the specific angles of the incident, transmitted and reflected waves (i , t and r , respectively). The dynamic properties are the relations between their amplitude, phase and polarization. The basic conservation law that governs the kinematic properties is the phase continuity of the electromagnetic field across the interface. The other conserved fields that determine the dynamic properties

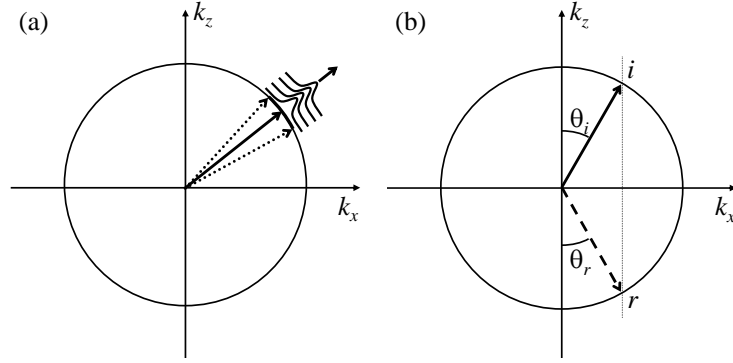


Figure A.1: (a) Diffraction of a confined optical beam (b) Plane wave reflection from a mirror surface

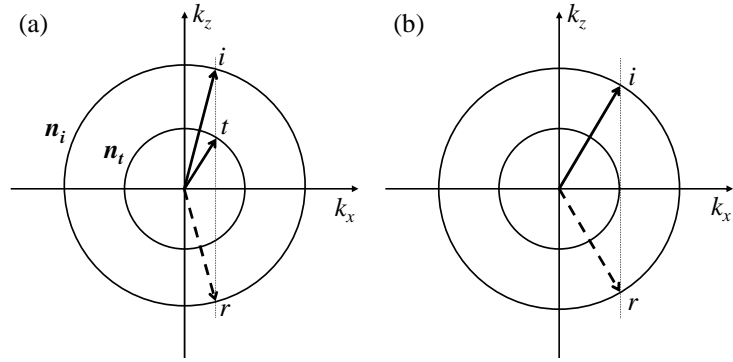


Figure A.2: (a) Plane wave refraction at the interface between two dielectric materials (b) The critical angle for total internal reflection

are the interface normal components of \vec{D} and \vec{B} and its parallel components of \vec{E} and \vec{H} .

Phase continuity along an interface is equivalent to conservation of the parallel component of k . If we assume, without loss of generality, the interface to lie along the \hat{x} -axis, the conserved component is k_x . Therefore, the only possible new plane waves after such interface crossing should have the same k_x component. It is now trivial to show that by hitting a mirror (Fig. A.1(b)), the only possible scattered waves are reflected at the incident angle $\theta_r = \theta_i$.

When the interface is between two transparent materials of different refractive indices, more waves are possible. Notice how the circle radius that describes the diffraction curve depends linearly on the material index. Thus, the passage introduces a second circle of a different radius (Fig. A.2(a)). We focus here on the case where $n_i > n_t$. The opposite case is a simple extension. The backward

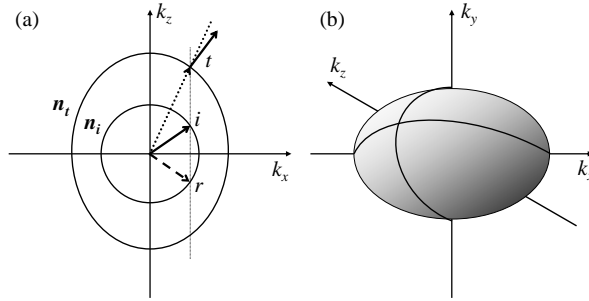


Figure A.3: **(a)** Beam refraction at a uniaxial crystal **(b)** Diffraction in the same crystal. The curvatures of $k_z(k_x)$ and $k_z(k_y)$ are different, resulting in beam deformation

wave in the new material is forbidden by infinity boundary condition, but two other waves are still possible. First, the reflected wave back into the incident material, as in the mirror case. The other is the transmitted wave into the new material. By conserving k_x while transferring to the inner circle, we see how the new transmitted wave has a new angle of propagation. Figure A.2(a) is a geometrical representation of Snell's law. Beyond a certain angle, there is no projection to the smaller circle, as presented in Fig. A.2(b). This angle is the critical angle above which Total Internal Reflection (TIR) occurs. It is geometrically trivial to show that the critical angle satisfies $\sin \theta_i = n_t/n_i$. On the other hand, a projection from the smaller circle to the larger, corresponding to a transition between low to high index materials, always exists. No TIR is possible in this case.

The diffraction relation approach generalizes the Snell's law, resulting in a very useful tool. In the context of this work, it can describe in a very simple way the deflection of a beam in a waveguide array due to sudden changes in the array parameters. Such changes can also occur on entering from and exiting the array to the continuum. A more common example for using it, though still quite a complex situation, is with refraction and diffraction in non-centrosymmetric crystals. For example, imagine an optical beam entering a uniaxial crystal. The polarization is in the plane of incidence, as is the crystal extraordinary axis (see Fig. A.3). In such a case, the light experiences a different refractive index (therefore a different k -number and phase) in every direction. The results are nontrivial. The beam would be deflected less (or more) than predicted by Snell because the diffraction slope is not perpendicular to the vector that connects it to the origin. More precisely, when the crystal is positive and the extraordinary axis is along the \hat{z} -axis or when the crystal is negative and the extraordinary axis is along the \hat{x} -axis, deflection will be reduced. In the other two cases, the beam deflection will be higher than expected by just implying Snell's law. Notice

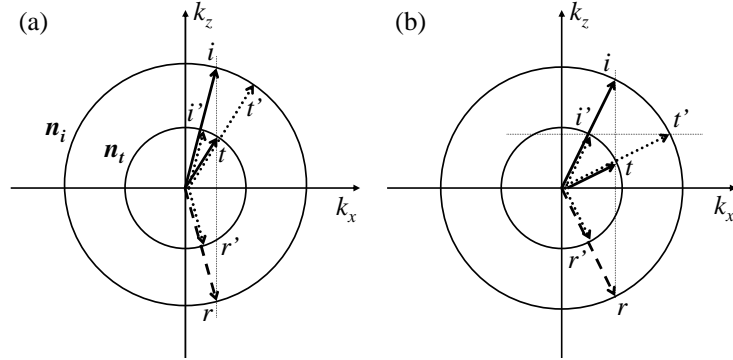


Figure A.4: (a) Vector definitions for the geometrical Fresnel relation representation (b) The Brewster angle for a polarization within the incidence plane

that the phase fronts will be still pointing in the Snell's direction, resulting in a mismatch between the phase vector and the Poynting vector.

Diffraction in uniaxial crystals is peculiar too. One consequence of this situation is that the curvatures of the diffraction relation, when the beam is on the \hat{z} -axis, differ between the \hat{x} and \hat{y} (out-of-plane) directions. Thus, an initially circular beam diffracts differently in the two dimensions. The result of such propagation is an elliptical deformation of the circular symmetric beam shape. Moreover, if the polarization is not linear and/or not aligned along a major axis, the two polarization components will diffract differently, leading to a complex polarization structure across the beam profile.

The dynamic properties of the interface crossing situation can also be derived geometrically from plots of the same kind (see Fig. A.4(a)). The justification for this derivation is less established though. Nevertheless, its simplicity is interestingly appealing. The problem is traditionally divided into two cases. The first is when the polarization of the incident light is perpendicular to the plane defined by the vectors i , t and r , i.e., the plane of incidence. In this case, we write the Fresnel relations using these vectors and then derive back the usual form:

$$\frac{E_r}{E_i} = \frac{[\vec{i} - \vec{t}]_z}{[\vec{t} - \vec{r}]_z} = \frac{n_i \cos \theta_i - n_t \cos \theta_t}{n_i \cos \theta_i + n_t \cos \theta_t}, \quad (\text{A.1})$$

$$\frac{E_t}{E_i} = -\frac{[\vec{i} - \vec{r}]_z}{[\vec{r} - \vec{t}]_z} = \frac{2n_i \cos \theta_i}{n_i \cos \theta_i + n_t \cos \theta_t}. \quad (\text{A.2})$$

$[\vec{v}]_z$ designates a projection of \vec{v} on the \hat{z} -axis. Although this projection is not necessary here because all vectors have the same k_x component, It will be required in the next case. Notice how the Fresnel relations are reconstructed using a simple and symmetrical form. It is very easy now to check that the two

boundary conditions are fulfilled by simple vector algebra.

$$E_i = E_t - E_r, \quad (\text{A.3})$$

$$E_i = \frac{n_t \cos \theta_t}{n_i \cos \theta_i} E_t + E_r. \quad (\text{A.4})$$

In order to write down the Fresnel relations for light polarization within the plane of incidence, we define some new vectors, marked by a tag (see Fig. A.4(a)). The principle is that a tagged vector is the intersection of the untagged vector with the circle of the other refractive index. Using this set of vectors, it is easy to show that the Fresnel relations can be written and derived back by:

$$\frac{E_r}{E_i} = \frac{[\vec{i}' - \vec{t}']_z}{[\vec{t}' - \vec{r}']_z} = \frac{n_t \cos \theta_i - n_i \cos \theta_t}{n_t \cos \theta_i + n_i \cos \theta_t}, \quad (\text{A.5})$$

$$\frac{E_t}{E_i} = -\frac{[\vec{i} - \vec{r}]_z}{[\vec{r} - \vec{t}]_z} = \frac{2n_i \cos \theta_i}{n_t \cos \theta_i + n_i \cos \theta_t}. \quad (\text{A.6})$$

Here again, the boundary conditions are verified vectorially:

$$E_i = \frac{n_t}{n_i} E_t - E_r, \quad (\text{A.7})$$

$$E_i = \frac{\cos \theta_t}{\cos \theta_i} E_t + E_r. \quad (\text{A.8})$$

The case of parallel polarization is known for the possibility of no reflected wave. The specific angle of incidence when all the light is passing through the interface is called the Brewster angle. We can see now in a geometrical way that in order for this to happen, \vec{i}' and \vec{t}' have to have the same height, or k_z components (see Fig. A.4(b)). It is possible to show geometrically that this condition can occur only when $\theta_i + \theta_t = \pi/2$, or equivalently $\tan \theta_i = n_t/n_i$. Beyond this angle, the reflection experiences a phase reversal as $[\vec{i}' - \vec{t}']_z$ becomes negative.

Diffraction curves can also describe the basic operation of some optical elements, such as gratings and prisms. Figure A.5(a) demonstrates the Bragg condition for scattering a plane wave off a grating with period of $2\pi/\Delta K$. The only possible angle is when the sum of the two vectors \vec{i}_1 and ΔK falls on an allowed plane wave of the same diffraction curve. For example, the i_2 wave can not be scattered by this grating. A different wavelength, having another curve radius, will have Bragg's condition fulfilled at another angle. In a more realistic case, a wide spectrum (with a range of curve radii) optical beam (having a range of k_x) is described as diffracting from a finite grating (thus of not well defined ΔK) in Fig. A.5(b). The properties of the diffracted beam can be derived from the intersection of all possibilities with the diffraction curve.

A prism is described as refraction at two consecutive angled interfaces. We recall that the possible k vectors after crossing an interface are those that conserve the parallel k component. Thus, as depicted in Fig. A.5(c), a plane wave i is first refracted into t_1 of the higher index. When exiting the prism glass, it is refracted again into t_2 . It is now possible to show geometrically (Fig. A.5(d))

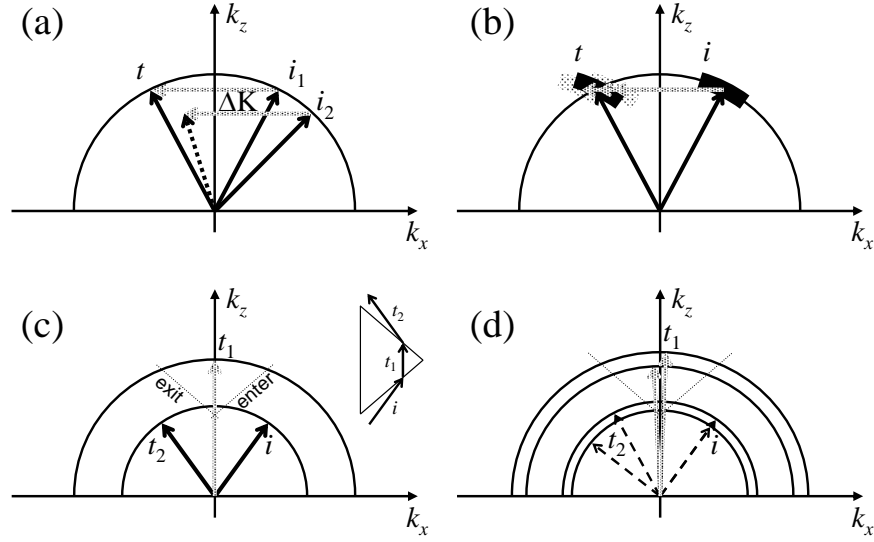


Figure A.5: (a) Bragg's condition for grating diffraction of plane waves. (b) A confined polychromatic beam diffracting on a finite grating. (c) A monochromatic plane wave passing through a prism. (d) Two wavelengths spatially dispersed in a prism

the difference in refraction of two wavelengths, initially having the same angle of propagation. When the index (curve radius) dependency on wavelength is only of $\propto 1/\lambda$, the two wavelengths are not separated. This can be proven easily by triangles similarity. It is only when the index of refraction changes quadratically with wavelength (dispersive glass), that the two plane waves are angularly separated at the prism output.

Appendix B

Spatiotemporal BPM Code

Here is an edited code from the simulation that was used in the planar glass spatiotemporal focusing experiment. The code is in the C computer language. A few parts are omitted such as some of the function bodies.

```
#define SIGN(a) ((a>=0) ? 1 : -1)
#define NX 256
#define NX2 512
#define NY 512
#define NZ 120000
#define AREA 131072
#define DIM 2
#define C 3e8

void fourn(double data[],unsigned long nn[],int ndim,int isign);
void phase(double [],double);
inline double power(double []);

double xposition(int);
double tposition(int);
void GetInitials(char *,double []);
void error(int,char *);

double grid_width,grid_length,z_length,beam_width,pulse_length,
       intensity,confocal_length,input_angle,input_center,wavelength,
       k0,n0,dn,n2,beta2,alpha6,
       omega2,tau1=12.2e-15,tau2=32e-15,
       *Pnl[2],*Ptemp;
int intervals=12;
```

```

int main(int argc, char *argv[]){

    double *data,temp,dz,dt,kx,w,td,tdr,pd[4],
           expr,sini,cosi,dz_const,dt_const;
    long i,j,k,z,p,td1,td2;
    unsigned long nn[DIM]={NX,NY}, nn2[1]={NY};

    if(argc!=2) error(1,"");

    // Memory allocation
    data=(double *)malloc(sizeof(double)*2*NX*NY);
    center=(double *)malloc(sizeof(double)*2*NY);
    Pnl[0]=(double *)malloc(sizeof(double)*2*NX*NY);
    Pnl[1]=(double *)malloc(sizeof(double)*2*NX*NY);
    if (!Pnl[1]) error(4,"");

    GetInitials(argv[1],data);

    // Pre-calculating constants
    dz=z_length/(NZ-0);
    dt=dz*n0/C;
    td=dt/(grid_length/NY);
    expr=exp(-dt/tau2), sini=sin(dt/tau1), cosi=cos(dt/tau1);
    td1=(int)td;
    td2=td1+1;
    tdr=td-td1;
    confocal_length=k0/2*beam_width*beam_width;
    omega2=(tau1*tau1+tau2*tau2)/tau1/tau1/tau2/tau2;
    dz_const=dz*k0*n2/(4e-6*grid_width/NX);
    dt_const=dt*tau1*omega2;
    pd[3]=0;

    // Start from scratch
    for(i=0;i<2*NX*NY;i++)
        Pnl[0][i]=Pnl[1][i]=0;

    // The main loop
    for(z=0;z<NZ;z++){

    // Fourier transform
        furn(data-1,nn-1,DIM,-1);

    // Dispersion and non-paraxial diffraction:
        for(j=0;j<NX;j++){
            kx=(double)j;
            if (kx>=NX/2) kx-=NX;

```

```

kx*=(2*PI/grid_width);
for(i=0;i<NY;i++){
  w=(double)i;
  if (w>=NY/2) w-=NY;
  w*=(2*PI/grid_length);
  if(abs(kx)<=k0*n0)
    phase(&data[2*(j*NY+i)]
          ,(sqrt(k0*k0*n0*n0-kx*kx)+0.5*w*w*beta2)*dz);
}
}

// Inverse Fourier transform
fourn(data-1,nn-1,DIM,1);

// Nonlinear absorbsion
for(i=0;i<NY;i++){
  for(j=0;j<NX;j++){
    data[2*(j*NY+i)]/=AREA;
    data[2*(j*NY+i)+1]/=AREA;
    temp=pow(power(&data[2*(j*NY+i)]),5);
    data[2*(j*NY+i)]*=
      exp(-dz*alpha6/2/(4e-6*grid_width/NX)*temp);
    data[2*(j*NY+i)+1]*=
      exp(-dz*alpha6/2/(4e-6*grid_width/NX)*temp);
  }
}

// Raman scattering:
for(j=0;j<NX;j++){
  for(i=0;i<NY-td2;i++){
    pd[2]=power(&data[2*(j*NY+i)]);
    Pnl[0][2*(j*NY+i)]=
      expr*(Pnl[1][2*(j*NY+i+td1)]*cosi
            -Pnl[1][2*(j*NY+i+td1)+1]*sini)+dt_const*pd[2];
    Pnl[0][2*(j*NY+i)+1]=
      expr*(Pnl[1][2*(j*NY+i+td1)]*sini
            +Pnl[1][2*(j*NY+i+td1)+1]*cosi);
    phase(&data[2*(j*NY+i)],dz_const
          *(0.2*Pnl[0][2*(j*NY+i)+1]+0.7*pd[2]));
  }
  Ptemp=Pnl[0]; Pnl[0]=Pnl[1]; Pnl[1]=Ptemp;
}
}

```

```

void GetInitials(char *fname,double data[]){

    char str[256];
    long i,j;
    double val;
    FILE *wgfile;

    // Open parameters file
    .
    .
    .

    // Initializing Beam
    for(i=0;i<NX;i++)
        for(j=0;j<NY;j++){
            data[2*(i*NY+j)]=sqrt(intensity*sqrt(2/PI)/beam_width)
                *exp(-xposition(i)*xposition(i)
                    /(beam_width*beam_width)
                    -tposition(j)*tposition(j)
                    /(pulse_length*pulse_length));
            data[2*(i*NY+j)+1]=0;
        }
    }

void phase(double ar[],double phi) {
    double temp;
    double cosphi=cos(phi),sinphi=sin(phi);

    temp=ar[0]*cosphi-ar[1]*sinphi;
    ar[1]=ar[0]*sinphi+ar[1]*cosphi;
    ar[0]=temp;
    }

inline double power(double com[]){
    return(com[0]*com[0]+com[1]*com[1]);
    }

double xposition(int i){
    return(grid_width*((double)(i+0.5)/(NX-1)-0.5));
    }

double tposition(int i){
    return(grid_length*((double)(i+0.5)/(NY-1)-0.5));
    }

```

Bibliography

- [1] A. Yariv, *Quantum Electronics*, 3rd edn. (John Wiley & Sons, New York 1988)
- [2] A.L. Jones, *J. Opt. Soc. Am.* **55**, 261 (1965)
- [3] S. Somekh, E. Garmire, A. Yariv, H.L. Garvin and R.G. Hunsperger, *Appl. Phys. Lett.* **22**, 46 (1973)
- [4] D.N. Christodoulides and R.I. Joseph, *Opt. Lett.* **13**, 794 (1988)
- [5] Y.S. Kivshar and M. Peyrard, *Phys. Rev. A* **46**, 3198 (1992)
- [6] Y.S. Kivshar, *Opt. Lett.* **18**, 1147 (1993)
- [7] Y.S. Kivshar and D.K. Campbell, *Phys. Rev. E* **48**, 3077 (1993)
- [8] W. Królikowsky, U. Trutschel, M. Cronin-Golomb and C. Schmidt-Hattenberger, *Opt. Lett.* **19**, 320 (1994)
- [9] A.B. Aceves, C. De Angelis, S. Trillo and S. Wabnitz, *Opt. Lett.* **19**, 332 (1994)
- [10] A.B. Aceves, C. De Angelis, T. Peschel, R. Muschall, F. Lederer, S. Trillo and S. Wabnitz, *Phys. Rev. E* **53**, 1172 (1996)
- [11] W. Królikowsky and Y.S. Kivshar, *J. Opt. Soc. Am. B* **13**, 876 (1996)
- [12] U. Peschel, R. Morandotti, J.S. Aitchison, H.S. Eisenberg and Y. Silberberg, *Appl. Phys. Lett.* **75**, 1348 (1999)
- [13] R. Muschall, C. Schmidt-Hattenberger and F. Lederer, *Opt. Lett.* **19**, 323 (1994)
- [14] I. Relke, *Phys. Rev. E* **57**, 6105 (1998)
- [15] A.B. Aceves, C. De Angelis, A.M. Rubenchik and S.K. Turitsyn, *Opt. Lett.* **19**, 329 (1994)
- [16] A.B. Aceves, C. De Angelis, G.G. Luther and A.M. Rubenchik, *Opt. Lett.* **19**, 1186 (1994)

- [17] A.B. Aceves, C. De Angelis, G.G. Luther, A.M. Rubenchik and S.K. Turitsyn, *Physica D* **87**, 262 (1995)
- [18] A.B. Aceves, G.G. Luther, C. De Angelis, A.M. Rubenchik and S.K. Turitsyn, *Phys. Rev. Lett.* **75**, 73 (1995)
- [19] Y.S. Kivshar, W. Królikowsky, and O.A. Chubyalo, *Phys. Rev. E* **50**, 5020 (1994)
- [20] M. Johansson and Y. Kivshar, *Phys. Rev. Lett.* **82**, 85 (1999)
- [21] S. Darmanyan, A. Kobayakov, E. Schmidt and F. Lederer, *Phys. Rev. E* **57**, 3520 (1998)
- [22] S. Darmanyan, A. Kobayakov and F. Lederer, *JEPT* **86**, 682 (1998)
- [23] Yu.S. Kivshar, A.R. Champneys, D. Cai and A.R. Bishop, *Phys. Rev. B* **58**, 5423 (1998)
- [24] W.P. Su, J.R. Schieffer, and A.J. Heeger, *Phys. Rev. Lett.* **42**, 1698 (1979)
- [25] A.S. Davydov, *Phys. Scr.* **20**, 387 (1979)
- [26] T. Holstein, *Ann. Phys.* **8**, 325 (1959); *Mol. Cryst. Liq. Cryst.* **77**, 235 (1981)
- [27] B. Denardo, B. Galvin, A. Greenfield, A. Larraza, S. Putterman, and W. Wright, *Phys. Rev. Lett.* **68**, 1730 (1992)
- [28] P. Marquii, J.M. Bilbaut, and M. Remoissenet, *Phys. Rev. E* **51**, 6127 (1995)
- [29] S. Flach and C.R. Willis, *Phys. Rep.* **295**, 182 (1998)
- [30] H.S. Eisenberg, Y. Silberberg, R. Morandotti, A.R. Boyd and J.S. Aitchison, *Phys. Rev. Lett.* **81**, 3383 (1998)
- [31] R. Morandotti, U. Peschel, J.S. Aitchison, H.S. Eisenberg and Y. Silberberg, *Phys. Rev. Lett.* **83**, 2726 (1999)
- [32] R. Morandotti, H.S. Eisenberg, Y. Silberberg, M. Sorel and J.S. Aitchison, *Phys. Rev. Lett.* **86**, 3296 (2001)
- [33] U. Peschel, T. Pertsch, and F. Lederer, *Opt. Lett.* **23**, 1701 (1998)
- [34] G. Lenz, I. Talanina and C.M. de Sterke, *Phys. Rev. Lett.* **83**, 963 (1999)
- [35] R. Morandotti, U. Peschel, J.S. Aitchison, H.S. Eisenberg and Y. Silberberg, *Phys. Rev. Lett.* **83**, 4756 (1999)
- [36] T. Pertsch, P. Dannberg, W. Elflein, A. Bräuer and F. Lederer, *Phys. Rev. Lett.* **83**, 4752 (1999)

- [37] H.S. Eisenberg, Y. Silberberg, R. Morandotti, and J.S. Aitchison, *Phys. Rev. Lett.* **85**, 1863 (2000)
- [38] S. Kawakami and H.A. Haus, *J. Light. Tech.* **4**, 160 (1986)
- [39] J.D. Jackson, *Classical Electrodynamics*, 3rd edn. (John Wiley & Sons, New York, 1998)
- [40] P.St.J. Russell, *Appl. Phys. B* **39**, 231 (1986)
- [41] P.St.J. Russell, *Phys. Rev. A* **33**, 3232 (1986)
- [42] N.W. Ashcroft and N.D. Mermin, *Solid State Physics* (Holt, Rinehart & Winston, New York 1976)
- [43] V.E. Zakharov and A.B. Shabat, *Zh. Eksp. Teor. Fiz.* **61**, 118 (1971)
[V.E. Zakharov and A.B. Shabat, *Sov. Phys. JEPT* 34, **62** (1972)]
- [44] A. Barthelemy, S. Maneuf and C. Froehly, *Opt. Commun.* **55**, 201 (1985)
- [45] J.S. Aitchison, Y. Silberberg, A.M. Weiner, D.E. Leaird, M.K. Oliver, J.L. Jackel, E.M. Vogel and P.W.E. Smith, *J. Opt. Soc. Am. B* **8**, 1290 (1990)
- [46] L.F. Mollenauer, R.H. Stolen and J.P. Gordon, *Phys. Rev. Lett.* **45**, 1095 (1980)
- [47] A.C. Scott and L. Macneil, *Phys. Lett. A* **98**, 87 (1983)
- [48] A.B. Aceves, C. De Angelis, A.M. Rubenchik and S.K. Turitsyn, *Opt. Lett.* **19**, 329 (1994)
- [49] C. Schmidt-Hattenberger, U. Trutschel, R. Muschall and F. Lederer, *Opt. Comm.* **82**, 461 (1991)
- [50] P. Millar, J.S. Aitchison, J.U. Kang, G.I. Stegeman, A. Villeneuve, G.T. Kennedy and W. Sibbett, *J. Opt. Soc. Am. B* **14**, 3224 (1997)
- [51] J.S. Aitchison, D.C. Hutchings, J.U. Kang, G.I. Stegeman and A. Villeneuve, *IEEE J. Quant. Elect.* **33**, 341 (1997)
- [52] Y. Silberberg, *Opt. Lett.* **15**, 1005 (1990)
- [53] G.P. Agrawal, *Nonlinear Fiber Optics* (Academic Press, San Diego 1995)
- [54] G.A. Swartzlander Jr., D.R. Andersen, J.J. Regan, Y. Hin, and A.E. Kaplan, *Phys. Rev.* **66**, 1583 (1991)
- [55] R. Morandotti, H.S. Eisenberg, D. Mandelik, Y. Silberberg, D. Modotto, M. Sorel and J. S. Aitchison, submitted
- [56] C. Zener, *Proc. R. Soc. London Ser. A* **145**, 523 (1932)

- [57] P. Nozieres and D. Pines, *The Theory of Quantum Liquids*, Vol. II (Addison Wesley, Redwood City, CA, 1990)
- [58] K. Staliunas, cond-mat 0205061 (2002)
- [59] P.W. Anderson, Phys. Rev. **109**, 1492 (1958)
- [60] N.F. Mott, Phil. Mag. **26**, 1015 (1972)
- [61] M.D. Feit and J.A. Fleck, Appl. Opt. **17**, 3990 (1978).
- [62] T. Pertsch, T. Zentgraf, U. Peschel, A. Braeuer and F. Lederer, Phys. Rev. Lett. **88**, 093901 (2002)
- [63] H. Kosaka, T. Kawashima, A. Tomita, M. Notomi, T. Tamamura, T. Sato and S. Kawakami, Appl. Phys. Lett. **74**, 1212 (1999)
- [64] L.G. Cohen, C. Lin and W.G. French, Electron. Lett. **15**, 334 (1979)
- [65] C. Lin, H. Kogelnik and L.G. Cohen, Opt. Lett. **5**, 476 (1980)
- [66] F.M. Knox, W. Forysiak and N.J. Doran, J. Lightwave Technol. **13**, 1955 (1995)
- [67] I.R. Gabitov and S.K. Turitsyn, Opt. Lett. **21**, 327 (1996)
- [68] M. Miyagi and S. Nishida, Apl. Opt. **18**, 678 (1979).
- [69] M.J. Ablowitz and Z. Musslimani, Phys. Rev. Lett. **87**, 254102-1 (2001)
- [70] R.W. Boyd, *Nonlinear Optics* (Academic Press, San Diego, 1992)
- [71] Y. Silberberg, Opt. Lett. **15**, 1282 (1990)
- [72] A.L. Dyshko, V.N. Lugovoi and A.M. Prokhorov, Sov. Phys. JETP **34**, 1235 (1972)
- [73] J.H. Marburger and E. Dawes, Phys. Rev. Lett. **21**, 556 (1968)
- [74] X. Liu, L.J. Qian and F.W. Wise, Phys. Rev. Lett. **82**, 4631 (1999)
- [75] I.G. Koprnikov, A. Suda, P. Wang and K. Midorikawa, Phys. Rev. Lett. **84**, 3847 (2000)
- [76] J.K. Ranka, R.W. Schirmer and A.L. Gaeta, Phys. Rev. Lett. **77**, 3783 (1996)
- [77] H.S. Eisenberg, R. Morandotti, Y. Silberberg, S. Bar-Ad, D. Ross and J.S. Aitchison, Phys. Rev. Lett. **87**, 043902-1 (2001)
- [78] A. Hasegawa and F. Tappert, App. Phys. Lett. **23**, 142 (1973); A. Hasegawa and F. Tappert, App. Phys. Lett. **23**, 171 (1973)

- [79] K.J. Blow and D. Wood, *J. Quant. Elect.* **25**, 2665 (1989)
- [80] R.J. Hawkins and C.R. Menyuk, *Opt. Lett.* **18**, 1999 (1993)
- [81] Y. Silberberg, *Opt. Lett.* **15**, 1005 (1990)
- [82] F.M. Mitschke and L.F. Mollenauer, *Opt. Lett.* **11**, 659 (1986)
- [83] J.P. Gordon, *Opt. Lett.* **11**, 662 (1986)
- [84] P. Beaud, W. Hodel, B. Zysset and H.P. Weber, *J. Quant. Elect.* **QE-23**, 1938 (1987)
- [85] P. Chernev and V. Petrov, *Opt. Lett.* **17**, 172 (1992); J.E. Rothenberg, *Opt. Lett.* **17**, 583 (1992)

Index

- AlGaAs, 11, 12, 19, 24
- Anderson Localization, 34
- Bessel function, 3
- Bloch oscillations, 31
- Brewster angle, 57
- Brillouin zone, 7, 31
- Catastrophic collapse, 43
- Coupled-mode theory, 3, 19, 35, 41
- Coupling length, 3
- Dark soliton, 25
- Diffraction, 53
 - anomalous, 24–26, 38
 - discrete, 3–8
 - linear, 3, 37
 - nonlinear, 7
 - length, 43, 44
 - management, 37
 - relation, 53
 - continuous, 5
 - discrete, 6
 - nonlinear, 8
- Discrete soliton, 8, 14
- Dispersion, 37, 43
 - length, 43, 44
- Floquet–Bloch wave function, 6, 31
- Fresnel relations, 56
- Kerr effect, 7
- Light bullets, 43, 44
- Localization parameter, 36
- Mode visibility, 15, 25, 33
- Multi-core fiber, 11
- Multi-photon absorption, 43, 44, 46, 48
- Peierls–Nabarro potential, 9, 21, 23
- Power steering, 21, 29, 37
- Pulse splitting, 44, 51
- Raman scattering, 44, 49
- Self-defocusing, 24–25
- Self-phase modulation, 19, 43
- Snell’s law, 55
- Spatial frequency, 5
- Two-photon absorption, 11, 12, 18
- Uniaxial crystal, 55
- Wannier–Stark states, 31

Epilog

To oblivion I shall disperse
said blue photon while he was depressed
No you won't, said his friend
I will not let us spread
Let's cheer up by the soliton dance

H.E.

תופעות אי-ליניאריות במערכים של מוליכי-גלים

תקציר

סוליטונים אופטיים נחקרים כבר כשלושים שנה. במהלך השנים הועלו הצעות לדוגמאות שונות של סוליטונים כאלה. חלקן אף הודגמו במעבדות במשך השנים. סוליטונים אופטיים מתחלקים לשתי משפחות ראשיות. הראשונה היא של סוליטונים במימד הזמן הנקראים סוליטונים זמניים. אלו הם פולסים של אור הנעים ללא ההתרחבות שנובעת באופן רגיל מנפיצת הצבע. הסוג השני הוא של סוליטונים מרחביים – קרני אור המתקדמות ללא דיפרקציה (התפשטות) בכיוון הניצב לתנועתן. הגורם המייצב בשני המקרים האלו הוא אחד – עוצמת אור גבוהה הגורמת לאפקט הקר האי-ליניארי.

תחום חדש שנחקר בעבודה זו הוא אופטיקה בדידה. באופן מסורתי, שדות אופטיים הם רציפים. לדוגמא, החתך של עוצמתה של קרן אור הוא פונקציה רציפה. ישנם מקרים בהם האור מאולץ לנוע במספר בדיד של אופנים המצומדים ביניהם. במקרים כאלו, התאור המלא של השדה האופטי הוא על-ידי אוסף בדיד של עוצמות. מקרה כזה המתקשר לעבודה זו הוא של מערך מוליכי-גלים חד-מימדיים, המונחים בקרבה כזו אחד לשני כך שהאור מצומד בין כל שני מוליכי-גלים שכנים. אור המוכנס למוליך גלים אחד יתפזר ויתפשט בין שאר הערוצים ככל שיתקדם במערך. להתפשטות זה יש קרבה גדולה באופן מתמטי לתופעת הדיפרקציה הגורמת להתפשטות שדות רציפים. לכן אנו מכנים אותה דיפרקציה בדידה.

אפקט הקר האי-ליניארי יכול למנוע גם את התרחבות התפלגות האור הבדידה כתוצאה מהדיפרקציה הבדידה. כתוצאה מתקדמים במערך מוליכי-גלים סוליטונים מרחביים בדידים. אנו היינו הראשונים להדגים היווצרות של סוליטונים כאלו בדגם עשוי אלומיניום-גליום-ארסניד. בהמשך חקרנו את התכונות של סוליטונים כאלה בתנועה לרוחב המערך. בתנועה כזו באות לידי ביטוי התוצאות של שבירת סימטרית ההסחה על-ידי מבנה המערך. עוד תופעה שנבדקה על-ידנו היא השפעת פגם במבנה המערך על סוליתון בדיד. הראנו גם שבתנאים מסוימים ניתן לעורר במערך מוליכי-גלים התפלגות אור שתורחב באופן אי-ליניארי במקום שתמוקד.

ההבנה שהשגנו על אופטיקה בדידה במהלך העבודה עם סוליטונים בדידים הובילה אותנו לערוך מספר ניסויים אחרים במערכי מוליכי-גלים. הראנו את תנודות בלון במערך שלרוחבו פוטנציאל ליניארי. בדקנו את השפעתם של פיזורים אקראיים (מיקום אנדרסון) על תופעת המיקוד האי-ליניארי. בנוסף הצענו שיטה לתכנון מוליכי-גלים בעלי תכונות דיפרקציה כלשהן בעזרת הצמדת מספר מערכים שונים.

פולסים של אור המציגים יציבות בשני המימדים (הזמן והמרחב) נקראים קליעי-אור. בפולסים אלו, אור המרוכז בנפח קטן שאינו משתנה מתקדמים באופן יציב. במהלך העבודה המוצגת כאן, הדגמנו תופעה זו בפעם הראשונה במוליך גלים משטחי עשוי סיליקה באמצעות אפקט הקר. הראנו שהתופעות הנוספות השולטות בהתפתחות פולסים כאלו הן בליעה אי-ליניארית ופיזור קָמֶן. כמו כן נכתבה תוכנה שדימתה באופן חישובי את ההתפתחות של פולסים אלו ושחזרה את כל התופעות החשובות שנצפו.